New Journal of Physics
The open access journal at the forefront of physics

Deutsche Physikalische Gesellschaft DPG IOP Institute of Physics

PAPER • OPEN ACCESS

Scaling theory for Mott–Hubbard transitions: I. $T = 0$ phase diagram of the 1/2-filled Hubbard model

To cite this article: Anirban Mukherjee and Siddhartha Lal 2020 *New J. Phys.* **22** 063007

New Journal of Physics
The open access journal at the forefront of physics

Deutsche Physikalische Gesellschaft DPG
IOP Institute of Physics

Published in partnership with: Deutsche Physikalische Gesellschaft and the Institute of Physics

OPEN ACCESS

RECEIVED
7 November 2019

REVISED
1 April 2020

ACCEPTED FOR PUBLICATION
9 April 2020

PUBLISHED
12 June 2020

PAPER

Scaling theory for Mott–Hubbard transitions: I. $T = 0$ phase diagram of the $1/2$-filled Hubbard model

Anirban Mukherjee and Siddhartha Lal

Department of Physical Sciences, Indian Institute of Science Education and Research-Kolkata, W.B. 741246, India

E-mail: am14rs016@iiserkol.ac.in and slal@iiserkol.ac.in

Keywords: Mott insulator, metal insulator transition, non-Fermi liquid, pseudogap, renormalisation group, topological order, quantum liquids

Supplementary material for this article is available online

Abstract

We present a $T = 0$K renormalization group (RG) phase diagram for the electronic Hubbard model in two dimensions on the square lattice at half filling. The RG procedure treats quantum fluctuations in the single particle occupation number nonperturbatively via the unitarily decoupling of one electronic state at every RG step. The resulting phase diagram thus possesses the quantum fluctuation energy scale (ω) as one of its axes. A relation is derived between ω and the effective temperature scale upto which gapless, as well as emergent gapped phases can be obtained. We find that the normal and insulating phases of the half-filled Hubbard model correspond, for any on-site repulsion, to a marginal Fermi liquid normal phase and a topologically-ordered gapped Mott insulating liquid respectively. The marginal Fermi liquid is found to arise from singular forward scattering in directions normal to the nested Fermi surface, while singular backscattering events lead to Mott liquid state. The transition between these two phases involves passage through a pseudogapped phase bookended by Fermi surface topology-changing Lifshitz transitions. The pseudogap phase is observed to arise from the electronic differentiation encoded within the nested Fermi surface, and involves the gradual gapping of the Fermi surface from antinodes to nodes via charge and spin excitations that are mutually entangled. We obtain effective Hamiltonians for various phases, as well as wavefunctions for the low-energy many-body eigenstates of the Mott liquid. Benchmarking of the ground-state energy per particle and the double-occupancy fraction for the Mott liquid against existing numerical results yields excellent agreement. Presence of a Néel ordering symmetry-breaking perturbation in the RG leads to an antiferromagnetic spin-ordered charge insulating Mott state. Our results thus offer novel insights on a variety of aspects of the Mott–Hubbard problem, and can be extended to the doped system.

1. Introduction

The nature of, and the transition into, the Mott insulating state defines a central problem in strongly correlated quantum matter. An analytically exact solution for the electronic Mott–Hubbard metal–insulator transition (MIT) exists only in one spatial dimension [1], while the status of the problem remains open in general. While the Mott insulator is often associated with a ($T = 0$) first order transition leading to a Neél antiferromagnetic ground state [2], the search continues for quantum liquid-like ground states corresponding to an insulating state that breaks no lattice or spin-space symmetries and is reached via a continuous transition. Indeed, there exist some theoretical proposals [3–6] as well as some experimental evidence for insulating spin-liquid ground states in layered organic conductors [7] and Herbertsmithite [8]. Recently, the metal–organic compound $Cu(DCOO)_2 \cdot 4D_2O$, an unfrustrated quasi two-dimensional antiferromagnet, was found to contain features of a resonating valence bond (RVB) like spin-liquid ground state [9].

Theoretical studies have not, however, identified unambiguously the order parameter for such correlation-driven metal–insulator transitions. The difficulties appear to be associated with an interplay of several complications: the fermion-sign problem limits some nonperturbative numerical investigations at low-temperatures [10], while many other numerical methods are either limited to small sizes or certain ranges in the coupling U/t (the ratio of the Hubbard repulsion to the nearest-neighbour hopping amplitude). It is, therefore, remarkable that a benchmarking exercise conducted on the 2D Hubbard model identified ranges in the values for the ground state energy per particle and the double occupancy fraction at specific values of the filling and U/t [11]. At the same time, a lack of an identifiable small parameter makes most analytic approaches beyond various mean-field schemes intractable when studying the problem at strong coupling.

Amidst these difficulties, several important questions related to the nature of the $T = 0$ phase diagram of the Mott–Hubbard transition, as well as the nature of the ground state, continue to be debated. For instance, we may ask: is there a critical value of the ratio U/t for the $T = 0$ Mott transition in the half-filled unfrustrated (i.e., with nearest neighbour hopping only) Hubbard model on a square lattice that corresponds to a paramagnetic state (i.e., with no magnetic order)? Studies using dynamical mean field theory (DMFT) [12–14] and quantum Monte Carlo [15] approaches indicate a first order transition at $T > 0$ ending at a critical $(U/t)_c$ at finite T. The status of the $T = 0$ metal–insulator transition remains to be understood. Further, the paramagnetic calculations can be interpreted as solutions for the case of vanishing inter-site correlations, and can presumably be trusted within only the (single-site) DMFT framework for the case of infinite dimensions.

The question, therefore, of whether the ground state of the two-dimensional Mott insulator at $T = 0$ possesses magnetic ordering or not needs further consideration. A reduction in the value of $(U/t)_c$ has also been observed in dynamical cluster approximation studies [16–18] as well as in cluster DMFT studies [19]. Recent studies involving the dynamical vertex approximation (DΓA) [20–22], auxillary field quantum Monte Carlo [22, 23], density matrix embedding theory [24] and ladder dual-fermion approach [25] have instead supported the existence of a gapped antiferromagnetic Néel state for all $U > 0$. Variational Monte Carlo studies using Gutzwiller projected wavefunctions have shown that a symmetry-preserved RVB state is energetically close to the symmetry-broken Néel antiferromagnetic state [4]. Upon including backflow correlations in the Gutzwiller projected wavefunctions, a nonmagnetic ground state [26] was found to exist at large values of U/t and sufficient frustration of the nearest neighbour hopping (t) by the addition of a next-nearest neighbour hopping (t'). This leaves open the question whether a nonmagnetic state can exist in the limit of $t' \to 0$ and weak coupling in U/t. Indeed, the variety of results obtained from various numerical methods demands an analytical approach that yields unambiguous insight into the nature of Mott insulating ground state of the 2D Hubbard model at $T = 0$, as well as the effective low-energy Hamiltonian that governs the low-lying excitations above this ground state. At the same time, a better view of the quantum metal–insulator transition involves understanding the nature of parent metallic state of the Mott insulator: is it a Fermi liquid with coherent Landau quasiparticle excitations, or some form of non-Fermi liquid involving collective excitations?

Noteworthy among efforts towards resolving this problem involves the application of the functional renormalization group (FRG) technique to the Mott transitions in the 2D Hubbard model (for reviews, see references [27, 28] and references therein). Results from FRG studies provide evidence for nodal-antinodal dichotomy [29]. Signatures of the strange metal and the pseudogap have also been reported within the FRG scheme [30–33]. FRG analysis of the 2D Hubbard model has also been successfully benchmarked against determinant quantum Monte Carlo simulations and the parquet approximation (PA) [34]. While the method is nonperturbative in principle, numerical implementations of the FRG have typically needed truncations at finite orders in the loop expansion. Thus, despite much success, the FRG is limited thus far to studying weak-to-intermediate values of U/t.

In this work, we present a novel Hamiltonian RG formalism in momentum space based on unitary transformations, and then employ it to develop a scaling theory for the 2D Hubbard model on a square lattice. We note that this model has earlier been studied using the continuous unitary transformation (CUT) RG formalism [35–38], rendered perturbative via a truncation at one-loop order. In contrast, we are able to conduct a nonperturbative study of the same model via our RG formalism. The groundwork for the RG is laid out in section 3. We initially derive the exact analytical form for the unitary operator that completely decouples one electronic state from the every other electronic degree of freedom. This is carried out by the removal of the appropriate off-diagonal blocks of the Hamiltonian represented in the occupation number basis of the state to be decoupled. The renormalized Hamiltonian is then shown to become block diagonal. For the case of the Hubbard model, the unitary rotations are applied iteratively on electronic states farthest away from the Fermi surface of the tight-binding part of problem, and gradually leading

towards its Fermi surface. This leads to an RG evolution in terms of an effective Hamiltonian, from which we have derived the RG flow equations for the 1-particle self energies, 2-particle vertices and 3-particle vertices. In comparison to the loop truncation approximations of the FRG scheme [28], we find nonperturbative RG equations of all 2-, 4-, and 6-point vertices, i.e., that have contributions from all loops resummed into closed-form expressions. Importantly, we find that the vertex RG flow happens across a family of quantum fluctuation scales (ω) that arise out of the noncommutativity between the kinetic energy term and the Hubbard onsite repulsion term. Indeed, this non-commutativity leads to number-density fluctuations of electronic states in momentum-space. As a direct outcome of the nonperturbative nature of the RG equations, we obtain stable fixed points of the flows at any given fluctuation scale ω. In this way, we are able to perform the RG analysis of the Hubbard model all the way from weak to strong coupling (in terms of the ratio of the Hubbard repulsion strength to the hopping amplitude, U/t). The effective Hamiltonian, and associated low-energy eigenstates, obtained at a stable fixed point then provides further avenues for analyses. This method is inspired by the strong-disorder RG approaches adopted by Dasgupta *et al* [39], Fisher [40], Rademaker–Ortuno [41] and You *et al* [42]. We have also recently used this RG technique to obtain a zero temperature phase diagram for the Kagome spin-1/2 *XXZ* antiferromagnet at non-zero magnetic field [43].

In section 4, we present the marginal Fermi liquid as the parent metal of the Mott insulating phase of the 2D Hubbard model at half-filling. We follow this in section 5 by detailing the journey through the pseudogap phase at half-filling, and the nature of the Mott–Hubbard MIT. In section 6, we present some features of topological order for the insulating Mott liquid phase obtained from the RG, as well as benchmark some of its properties with the numerical results obtained from references [11, 44, 45]. We also demonstrate how an RG relevant symmetry breaking perturbation leads to the Néel antiferromagnetic Mott state. Finally, we conclude our presentation in section 7 with a detailed discussion of the relevance of our work to Mott insulating systems, and by presenting future perspectives. Further details of the derivations of various RG relations are presented in the appendices.

2. Summary of main results

- *Normal state corresponding to the* $1/2$*-filled Mott insulator*: we establish the marginal Fermi liquid (MFL) as the parent normal state of the $1/2$-filled Mott insulating state of the 2D Hubbard model. This novel gapless state of quantum matter obtains from singular forward scattering events that destabilise Landau quasiparticles, establishing instead composite 2 electron–1 hole excitations as long-lived in the proximity of the Fermi surface. We derive an effective Hamiltonian for the MFL, as well as provide comprehensive insight into the microscopic origins of various aspects of the well-known MFL phenomenology.
- *Pseudogap state at* $1/2$*-filling*: by tracking the dynamical transfer of spectral weight under RG, we demonstrate that the Mott transition is continuous in nature and involves passage through a pseudogap (PG) phase, i.e., a phase in which the neighbourhood of the Fermi surface is progressively gapped out from the antinodal (AN) regions to the nodal (N) regions. The entry into and exit from the PG phase involve two Fermi surface topology-changing interacting Lifshitz transitions of the marginal Fermi liquid at the AN and N points respectively. The PG phase is shown to be characterised by a novel topological quantum number distinct from the MFL and Mott insulating phases. Additional evidence is presented in video S1 (https://stacks.iop.org/NJP/22/063007/mmedia).
- *Mott liquid insulating state* $1/2$*-filling*: we demonstrate the existence of a symmetry preserved Mott liquid insulating state at $1/2$-filling with signatures of topological order. We also show that this quantum liquid develops into the Neel antiferromagnet Mott insulator upon symmetry breaking. This appears to provide, within the context of a Hubbard model, an explicit and detailed substantiation of Anderson's conjecture [46] for the Néel antiferromagnetic Mott insulator observed experimentally in the cuprates as having their origin in a novel quantum liquid state of matter. The ground state energy per site is obtained for the Mott liquid from a finite-sized scaling analysis, and benchmarked against existing numerical results for $2 \leqslant U/t \leqslant 12$, displaying excellent agreement and imparting confidence in the effective Hamiltonian and ground state wavefunction obtained from the RG analysis. Codes used in the benchmarking have been made available electronically [47].

3. Renormalization group scheme

We analyse the Hubbard model on the two-dimensional square lattice with nearest neighbour hopping (strength t) and on-site repulsion (strength U_0)

$$\hat{H} = \sum_{\mathbf{k},\sigma} (\epsilon_{0\mathbf{k}} - \mu_{\text{eff}}) c^{\dagger}_{\mathbf{k}\sigma} c_{\mathbf{k}\sigma} + U_0 \sum_{\mathbf{r}} \hat{\tau}_{\mathbf{r}\uparrow} \hat{\tau}_{\mathbf{r}\downarrow}\,, \tag{1}$$

where $c^{\dagger}_{\mathbf{k}\sigma}/c_{\mathbf{k}\sigma}$ is the electron creation/annihilation operator with wave-vector $\mathbf{k}$ and spin σ, $\hat{\tau}_{\mathbf{r}\sigma} = \hat{n}_{\mathbf{r}\sigma} - \frac{1}{2}$, $\hat{n}_{\mathbf{r}\sigma} = c^{\dagger}_{\mathbf{r}\sigma} c_{\mathbf{r}\sigma}$ is the number operator at lattice site , and $\epsilon_{0\mathbf{k}}$ is the bare dispersion. The effective chemical potential, $\mu_{\text{eff}} = \mu - \frac{U_0}{2}$, accounts for the energy imbalance between doublons (doubly occupied sites) and holons (empty sites). The hopping term is clearly diagonal in momentum-space, with a dispersion for the square lattice given by $\epsilon_{0\mathbf{k}} = -2t(\cos k_x + \cos k_y)$. On the other hand, the Hubbard repulsion term is diagonal in real-space, i.e., it contains off-diagonal elements in the momentum basis causing fluctuations in the dispersion ($\Delta(\epsilon_{\mathbf{k}\sigma}\hat{n}_{\mathbf{k}\sigma})$). Below, we will reveal the effects of such quantum fluctuations via a Hamiltonian renormalization group (RG) method. Further, we will study the Mott metal–insulator transition (MIT) at 1/2-filling, i.e., by setting the doublon–holon chemical potential $\mu^0_{\text{eff}} = \mu - \frac{U_0}{2} = 0$ [48, 49]. In subsection 3.1, we first derive the form of the exact unitary disentanglement operator that causes the one-step decoupling of a single electronic state. Then, we compute the form of the rotated Hamiltonian resulting from this transformation. We follow this in subsection 3.2 by adapting a successive set of such unitary operations on the Hamiltonian into an RG scheme. In this scheme, the states with the highest bare electronic kinetic energy $\epsilon_{\mathbf{k}\sigma}$ are the first to be exactly decoupled. This is followed by exactly decoupling the next highest $\epsilon_{\mathbf{k}\sigma}$, thus gradually scaling towards the Fermi surface. In subsection 3.3, we give a detailed description of the relation between the quantum fluctuation energyscale ω that appears in our RG formalism, and an equivalent thermal scale. We then present a discussion of instabilities of the Fermi surface in subsection 3.4, and follow it with a detailed derivation of various RG relations for the 2D Hubbard model in subsection 3.5.

3.1. Derivation of unitary operator for one-step decoupling of an electronic state

The RG procedure is carried out by decoupling one single-particle state $\mathbf{k}\sigma\rangle$ at every RG step via a unitary operation $U_{\mathbf{k}\sigma}$

$$\hat{n}_{\mathbf{k}\sigma} U_{\mathbf{k}\sigma} \hat{H} U^{\dagger}_{\mathbf{k}\sigma} (1 - \hat{n}_{\mathbf{k}\sigma}) = 0 \rightarrow [\hat{n}_{\mathbf{k}\sigma}, U_{\mathbf{k}\sigma} \hat{H} U^{\dagger}_{\mathbf{k}\sigma}] = 0\,, \tag{2}$$

thereby trivializing the non-commutativity relation $[\hat{n}_{\mathbf{k}\sigma}, \hat{H}] \neq 0$ for the decoupled state. Below we derive the form for $U_{\mathbf{k}\sigma}$ that satisfies equation (2). The equation equation (2) can equivalently be written as $P_{\mathbf{k}\sigma}\hat{H}(1 - P_{\mathbf{k}\sigma}) = 0$ where $P_{\mathbf{k}\sigma} = U^{\dagger}_{\mathbf{k}\sigma} \hat{n}_{\mathbf{k}\sigma} U_{\mathbf{k}\sigma}$, is the rotated projection operators. With these operators we define a new Hamiltonian $\bar{H} = P_{\mathbf{k}\sigma}\hat{H}P_{\mathbf{k}\sigma}$. Then the decoupling equation equation (2) amounts to solving

$$\hat{H}|\Psi\rangle = \bar{H}|\Psi\rangle, \tag{3}$$

where $|\Psi\rangle$ satisfies the condition: $P_{\mathbf{k}\sigma}|\Psi\rangle = |\Psi\rangle$. In order to show clearly that certain terms in the rotated Hamiltonian vanish and lead to equation (2), we decompose the Hamiltonian H into diagonal and off-diagonal pieces: $\hat{H} = H^D + H^X_{\mathbf{k}\sigma} + H^X_{\bar{\mathbf{k}}\sigma}$. The diagonal piece ($H^D$) constitutes the 1-particle dispersion and 2-particle density-density (Hartree–Fock) terms. The second term, $H^X_{\mathbf{k}\sigma}$, represents the off-diagonal coupling between state $|\mathbf{k}\sigma\rangle$ and other momentum states states $|\mathbf{k}'\sigma'\rangle$. Finally, the third piece ($H^X_{\bar{\mathbf{k}}\sigma}$) represents the off-diagonal coupling among all momentum states other than $|\mathbf{k}\sigma\rangle$. Solving equation (2) is then equivalent to finding a state $|\Psi\rangle$ such that

$$(H^D + H^X_{\mathbf{k}\sigma} + H^X_{\bar{\mathbf{k}}\sigma})|\Psi\rangle = \bar{H}|\Psi\rangle, \tag{4}$$

where $\bar{H} = H'^D + H'^X_{\mathbf{k}\sigma}$. Here H'^D and $H'^X_{\mathbf{k}\sigma}$ have similar definitions as given above for H^D and $H^X_{\mathbf{k}\sigma}$ respectively. To proceed, we write $|\Psi\rangle$ in a Schmidt decomposed form

$$|\Psi\rangle = a_1|\Psi_1, 1_{\mathbf{k}\sigma}\rangle + a_0|\Psi_0, 0_{\mathbf{k}\sigma}\rangle. \tag{5}$$

In the above expression, the occupation number states $|1_{\mathbf{k}\sigma}\rangle$, $|0_{\mathbf{k}\sigma}\rangle$ comprise a two-dimensional Hilbert space and the orthogonal states $|\Psi_1\rangle$ and $|\Psi_0\rangle$ ($\langle\Psi_0|\Psi_1\rangle = 0$) belong to the remnant 2^{N-1} dimensional Hilbert space of $1, \ldots, N-1$ single-electron degrees of freedom. Then, the decoupling equation (equation (2)) connects the elements in $|\Psi\rangle$ as follows

$$a_1|\Psi_1, 1_{\mathbf{k}\sigma}\rangle = a_0\eta^{\dagger}_{\mathbf{k}\sigma}|\Psi_0, 0_{\mathbf{k}\sigma}\rangle,\; a_0|\Psi_0, 0_{\mathbf{k}\sigma}\rangle = a_1\eta_{\mathbf{k}\sigma}|\Psi_1, 1_{\mathbf{k}\sigma}\rangle\,, \tag{6}$$

where the operator $\eta_{\mathbf{k}\sigma}$ is defined as

$$\eta_{\mathbf{k}\sigma} = \frac{1}{\hat{\omega} - \mathrm{Tr}_{\mathbf{k}\sigma}(H^D(1-\hat{n}_{\mathbf{k}\sigma}))(1-\hat{n}_{\mathbf{k}\sigma})}\mathrm{Tr}_{\mathbf{k}\sigma}(c^\dagger_{\mathbf{k}\sigma}H)c_{\mathbf{k}\sigma}, \tag{7}$$

and $\hat{\omega} = H'^D + H'^X_{\mathbf{k}\sigma} - H^X_{\mathbf{k}\sigma}$. Further, the definition of $\hat{\omega}$ implies the commutation $[\hat{\omega}, \hat{n}_{\mathbf{k}\sigma}] = 0$, resultingly its eigenstates are labelled by good quantum numbers $1_{\mathbf{k}\sigma}, 0_{\mathbf{k}\sigma}$. This result will be important later. Here, $\mathrm{Tr}_{\mathbf{k}\sigma}(\cdot)$ stands for a partial trace in the Fock space. Using equation (6), we arrive at $\eta^\dagger_{\mathbf{k}\sigma}\eta_{\mathbf{k}\sigma} = \hat{n}_{\mathbf{k}\sigma} = 1 - \eta_{\mathbf{k}\sigma}\eta^\dagger_{\mathbf{k}\sigma}$ leading to the algebraic relations

$$\{\eta^\dagger_{\mathbf{k}\sigma}, \eta_{\mathbf{k}\sigma}\} = 1, [\eta^\dagger_{\mathbf{k}\sigma}, \eta_{\mathbf{k}\sigma}] = 2\hat{n}_{\mathbf{k}\sigma} - 1, \eta^2_{\mathbf{k}\sigma} = 0. \tag{8}$$

Also, we note that using equations (6) and (8) together with the form of the state $|\Psi\rangle$ (equation (5)), we obtain a similarity transformation between $|\Psi_1, 1_{\mathbf{k}\sigma}\rangle$ and $|\Psi\rangle$

$$a_0|\Psi_0, 0_{\mathbf{k}\sigma}\rangle = a_1\eta_{\mathbf{k}\sigma}|\Psi_1, 1_{\mathbf{k}\sigma}\rangle \Rightarrow |\Psi\rangle = a_1(1+\eta_{\mathbf{k}\sigma})|\Psi_1, 1_{\mathbf{k}\sigma}\rangle = a_1\ \exp(\eta_{\mathbf{k}\sigma})|\Psi_1, 1_{\mathbf{k}\sigma}\rangle. \tag{9}$$

Importantly, in the many-body state $|\Psi_1, 1_{\mathbf{k}\sigma}\rangle$, the single electronic state labelled $\mathbf{k}\sigma$ is disentangled. From this similarity transformation, we can construct the $U_{\mathbf{k}\sigma}$ [50, 51]

$$U_{\mathbf{k}\sigma} = \exp\frac{\pi}{4}(\eta^\dagger_{\mathbf{k}\sigma} - \eta_{\mathbf{k}\sigma}) = \frac{1}{\sqrt{2}}(1 + \eta^\dagger_{\mathbf{k}\sigma} - \eta_{\mathbf{k}\sigma}), \tag{10}$$

that transforms $|\Psi\rangle$ to $|\Psi_1, 1_{\mathbf{k}\sigma}\rangle = U|\Psi\rangle$. The unitarity property $U_{\mathbf{k}\sigma}U^\dagger_{\mathbf{k}\sigma} = U^\dagger_{\mathbf{k}\sigma}U_{\mathbf{k}\sigma} = I$ can be verified using the algebra of $\eta_{\mathbf{k}\sigma}$ and $\eta^\dagger_{\mathbf{k}\sigma}$ operators given in equation (8). Finally the application of $U_{\mathbf{k}\sigma}$ on H leads to the rotated Hamiltonian,

$$U_{\mathbf{k}\sigma}HU^\dagger_{\mathbf{k}\sigma} = \frac{1}{2}\mathrm{Tr}_{\mathbf{k}\sigma}(H) + \tau_{\mathbf{k}\sigma}\mathrm{Tr}_{\mathbf{k}\sigma}(H\tau_{\mathbf{k}\sigma}) + \tau_{\mathbf{k}\sigma}\{c^\dagger_{\mathbf{k}\sigma}\mathrm{Tr}_{\mathbf{k}\sigma}(Hc_{\mathbf{k}\sigma}), \eta_{\mathbf{k}\sigma}\}. \tag{11}$$

One can easily check that $[U_{\mathbf{k}\sigma}HU^\dagger_{\mathbf{k}\sigma}, \hat{\tau}_{\mathbf{k}\sigma}] = 0$, i.e., $\tau_{\mathbf{k}\sigma}$ is an integral of motion. Turning to the quantum fluctuation operator $\hat{\omega}$, we note that its eigenvalues represent energy scales for occupation number fluctuations of state $|\mathbf{k}\sigma\rangle$.

We can now put our unitary disentangling tranformation in context with the canonical transformations used in various other RG methods, including continuous unitary transformation (CUT) RG [35–37, 52], strong disorder RG [41, 53] and spectrum bifurcation RG [42]. All of these RG schemes aim to make the Hamiltonian more and more diagonal at every RG step like CUT RG , entanglement CUT RG scheme [54] aim to make it band diagonal. Similarly the recent strong disorder RG schemes [41, 42, 53, 55] aim to make the Hamiltonian block diagonal. Nevertheless, this implementation of the unitary RG eventually becomes perturbative in nature due to truncation of infinite coupling expansion to finite loop orders.

This should be contrasted with the closed-form analytic expressions for the rotated block daigonal Hamiltonian obtained at each RG step thus avoiding issues with loop truncation. Further we provide an exact prescription for reaching stable fixed points [56]: *one of the energy eigenvalues of $\hat{\omega}$ operator matches with an eigenvalue of the diagonal operator H^D, resultingly $H^X_{\mathbf{k}\sigma}$ vanishes*. This can be seen as follows: from the discussion below equation (7), we note that any eigenstate of $\hat{\omega}$ can be written as $|\Phi_1, 1_{\mathbf{k}\sigma}\rangle$. Next, from the relations: $\hat{n}_{\mathbf{k}\sigma} = \eta^\dagger_{\mathbf{k}\sigma}\eta_{\mathbf{k}\sigma}$, $\hat{n}_{\mathbf{k}\sigma}|\Phi_1, 1_{\mathbf{k}\sigma}\rangle = |\Phi_1, 1_{\mathbf{k}\sigma}\rangle$ we obtain,

$$\begin{aligned}\eta^\dagger_{\mathbf{k}\sigma}\eta_{\mathbf{k}\sigma}|\Phi_1, 1_{\mathbf{k}\sigma}\rangle &= |\Phi_1, 1_{\mathbf{k}\sigma}\rangle,\\ (\omega - \mathrm{Tr}_{\mathbf{k}\sigma}(H^D\hat{n}_{\mathbf{k}\sigma})\hat{n}_{\mathbf{k}\sigma})|\Phi_1, 1_{\mathbf{k}\sigma}\rangle &= c^\dagger_{\mathbf{k}\sigma}\ \mathrm{Tr}(Hc_{\mathbf{k}\sigma})\eta_{\mathbf{k}\sigma}|\Phi_1, 1_{\mathbf{k}\sigma}\rangle.\end{aligned} \tag{12}$$

If ω matches with any diagonal entry of $\mathrm{Tr}_{\mathbf{k}\sigma}(H^D\hat{n}_{\mathbf{k}\sigma})\hat{n}_{\mathbf{k}\sigma}$ then,

$$Det(\omega - \mathrm{Tr}_{\mathbf{k}\sigma}(H^D\hat{n}_{\mathbf{k}\sigma})\hat{n}_{\mathbf{k}\sigma}) = 0. \tag{13}$$

In order for equation (12) to have a solution, the right-hand side of equation (12) must also vanish. The *nessecary* and *sufficient* condition for RHS to vanish is: $\eta_{\mathbf{k}\sigma} = 0$, that implies $c^\dagger_{\mathbf{k}\sigma}\ \mathrm{Tr}(Hc_{\mathbf{k}\sigma})\eta_{\mathbf{k}\sigma} = 0$, hence $H^X_{\mathbf{k}\sigma} = c^\dagger_{\mathbf{k}\sigma}\ \mathrm{Tr}(Hc_{\mathbf{k}\sigma}) + \mathrm{h.c.} = 0$.

In the next section, we implement the unitary transformations $U_{\mathbf{k}\sigma}$'*s* iteratively on the Hubbard Hamiltonian (equation (1)) by progressively decoupling the highest energy state $\epsilon_{\mathbf{k}\sigma}$, and scaling gradually towards the Fermi energy E_F. This allows us to set up a momentum-space Hamiltonian RG theory [43] for the 2D Hubbard model (figure 1).

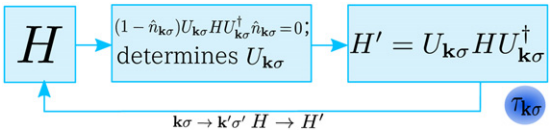

Figure 1. Schematic diagram of the iterative unitary RG procedure. At each RG step, a commuting operator $\tau_{\mathbf{k}\sigma}$ (blue circle) is generated.

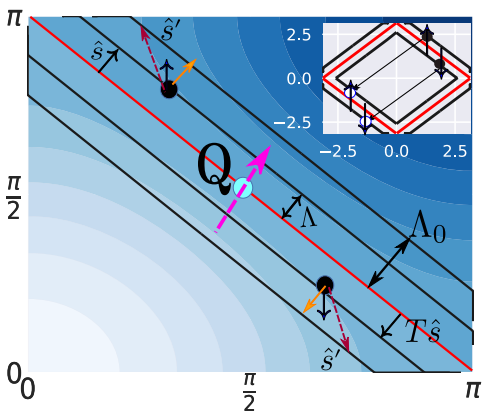

Figure 2. Schematic representation of shells [black lines parallel to and formed around the FS (red line)] of states that are integrated out from first quadrant of Brillouin zone (BZ): $0 < k_x, k_y < \pi$. The black dots represents a pair of opposite spin electronic states. $\hat{s}$ represents the direction normal to F, the orange arrows represent the forward scattering process. $T\hat{s} = (s_y, s_x)$ represents the orientation vector symmetrically placed about the nodal vector $\mathbf{Q}$ (pink arrow). The pair of brown dashed lines shows tangential scattering from $\hat{s}, T\hat{s} \to \hat{s}', T\hat{s}'$. Inset (top right): Umklapp scattering of electron pairs.

3.2. RG via the decoupling of single-particle occupation states

In this section, we design the RG scheme that implements the algorithm shown in figure 1 for decoupling single-particle Fock states. We will define shells that are isogeometric to the non-interacting Fermi surface (see figure 2). This involves identifying the Fermi surface of the half-filled tight-binding model on the 2D square lattice at $E_{\rm F} = \mu^0_{\rm eff} = 0$. The Fermi surface (FS) is then defined as a collection of unit normal wave-vectors $\hat{s} = \nabla\epsilon_{\mathbf{k}}/|\nabla\epsilon_{\mathbf{k}}\|_{\epsilon_{\mathbf{k}}=E_{\rm F}}$. The C_4 symmetric square FS also has four van-Hove singularities along the antinodal (AN) directions: two along $\mathbf{Q}_y = (0, \pi)$ and another two along $\mathbf{Q}_x = (\pi, 0)$ (figure 2). The nodal (N) directions are given by the bisectors: $\mathbf{Q} = \mathbf{Q_x} + \mathbf{Q_y}$ and $\mathbf{Q}_\perp \perp \mathbf{Q}$. The normal vectors are defined as $\hat{s} = \mathbf{Q}/|\mathbf{Q}|$ on one quadrant of the square Fermi surface, which on crossing the van-Hove to the other arm becomes orthogonally oriented to $\hat{s}$: $\hat{s}_\perp = \mathbf{Q}_\perp/|\mathbf{Q}_\perp|, \hat{s}_\perp \cdot \hat{s} = 0$.

The normal translations of the Fermi surface wave-vectors $\mathbf{k}_{\Lambda,\hat{s}} = \mathbf{k}_{\rm F}(\hat{\mathbf{s}}) + \Lambda\hat{\mathbf{s}}$ represent *isogeometric curves* displaced parallel by distance Λ from the FS (i.e., the black lines parallel to the FS shown in figure 2(a)). Importantly, the anisotropy of the dispersion term with $\hat{s}$ on the Fermi surface ($k_{{\rm F}x} + k_{{\rm F}y} = \pi$), together with the non-commutativity of the hopping and onsite U term, leads to a variety of quantum fluctuation scales ranging from the anti-nodes (AN: $k_{{\rm F}x} = 0$) to the nodes (N: $k_{{\rm F}x} = \pi/2$). Given the redefinition of the electronic wave vectors in terms of Λ and $\hat{s}$, we will devote a few lines to describe the labelling scheme. States are ordered in terms of distances $\Lambda_N > \cdots > \Lambda_j > \Lambda_{j-1} > \cdots > 0$, where Λ_N lies near the Brillouin zone (BZ) edge and the smallest Λ is proximate to the Fermi surface. Followingly this construction, the electronic states are labelled equivalently as $|j, l\rangle \equiv |\mathbf{k}_{\Lambda_j\hat{s}}\sigma\rangle (l = \{\hat{s}, (\sigma = \uparrow, \downarrow)\})$. By employing unitary transformations iteratively, the RG disentangles electronic states in shells, starting from near the BZ edge and scaling towards $E_{\rm F}$. Thus, at step j, all the states on the curve labelled by Λ_j are disentangled via a unitary rotation $U_{(j)}$. The resulting Hamiltonian $H_{(j-1)} = U_{(j)}H_{(j)}U^\dagger_{(j)}$ is off-diagonal only for states with $\Lambda < \Lambda_j$.

The momentum-space representation of the Hubbard term contains four-fermionic off-diagonal scattering pieces coupling states between isogeometric curves (longitudinal scattering), and between normal directions $\hat{s}$ (tangential scattering). Thus, the renormalization group (RG) flow takes place via the decoupling of an isogeometric curve (Λ_j) farthest from the FS at every step by using a product of unitary operations ($U_{(j)}$), itself a product of unitary operators $U_{(j,l)}$ that decouple individual states $(j, l) \equiv (\mathbf{k}_{\Lambda_j\hat{s}}, \sigma)$

along a given normal $\hat{s}$

$$U_{(j)} = \prod_{l=(\hat{s},\sigma)} U_{(j,l)}\,,\; U_{(j,l)} = \frac{1}{\sqrt{2}}[1 + \eta^{\dagger}_{(j,l)} - \eta_{(j,l)}]. \tag{14}$$

Here $\eta_{(j,l)}$ is defined as in equation (7) and $\eta^{\dagger}_{(j,l)}$ is the hermitian conjugate.

The flow equation for the Hamiltonian is then given by

$$H_{(j-1)} = U_{(j)} H_{(j)} U^{\dagger}_{(j)}, \tag{15}$$

where the count of RG step j involves a countdown from N (the number of isogeometric curves from the BZ boundaries to FS), such that the bare Hamiltonian $H \equiv H_{(N)}$. In a later section, we show the method for obtaining the vertex RG flow equations using the form of the rotated Hamiltonian like that obtained in equation (11).

3.3. Correspondence between ω and an emergent thermal scale *T*

In the above RG scheme the renormalized Hamiltonian can be decomposed over all fluctuation scales as follows $H_{(j)} = \sum_{\omega}(H_{(j)}(\omega)\hat{O}(\omega))_{(j)}$, where $\hat{O}(\omega)_{(j)}$ projects onto an eigensubspace of $\hat{\omega}$ with fluctuation energy eigenvalue ω. A variety of many body correlations can be encoded within the various $H_{(j)}(\omega)$'s describing different subspaces of the many body spectrum. Can the effects of ω dependent many body correlations on the non-interacting Fermi gas at 0 K be manifested in a finite temperature T scale?

We now proceed to find the relation between the thermal energy $k_{\mathrm{B}}T$ and energy broadening due to the virtual excitations of the quasiparticle. These virtual excited states drive the RG flow. Resultingly an effective Hamiltonian $H_{>j} = \mathrm{Tr}_{1,\ldots,j}(H_{(j)})$ comprising the excited states decoupled under RG flow is obtained by partial tracing $H_{(j)}$ over the remnant coupled degrees of freedom ($\tau_j = \hat{n}_j - \frac{1}{2}$),

$$H_{>j}(\omega_i) = \sum_{j_1>j} \tilde{\epsilon}_{j_1}(\omega_i)\tau_{j_1} + \sum_{j_1,j_2>j} \Gamma^4_{j_1,j_2}(\omega_i)\tau_{j_1}\tau_{j_2} + \sum_{j_1,j_2,j_3>j} \Gamma^6_{j_1,j_2,j_3}(\omega_i)\tau_{j_1}\tau_{j_2}\tau_{j_3} + \cdots \tag{16}$$

where $\tilde{\epsilon}_j(\omega_i) = \epsilon_j + \Sigma_j(\omega_i)$ with Σ_j composed of all higher order correlations. Given that we are unitarily disentangling precisely one single-particle state at every RG step, a thermal scale arises by limiting our perspective to many-body correlations within the single-particle Hamiltonian $\sum_{j_1}\epsilon_j(\omega_i)\tau_{j_1}$.

For this Hamiltonian, we introduce the imaginary-time evolution operator $U^1_{(j)}(\tau) = \exp(-\tau\sum_{j_1>j}\tilde{\epsilon}_{j_1}(\omega_i)\tau_{j_1})$ fulfiling the Kubo–Martin–Schwinger (KMS) condition $U^1_{(j)}(\tau) = -U^1_{(j)}(\tau+\beta)$ for fermions [57], $\beta = (k_{\mathrm{B}}T)^{-1}$ is the imaginary-time period. The KMS condition allows us to attain a Matsubara spectral representation for $U^1_{>j}$ (where $\tilde{\omega}_m = \frac{\pi(2m+1)}{\beta}$ are the harmonics)

$$U^1_{>j}(\mathrm{i}\tilde{\omega}_m, \omega) = \sum_{\beta} \mathrm{e}^{\tau\tilde{\omega}_m}\tilde{U}^1_{>j}(\tau,\omega) = \sum_{l=j+1}^{N} \frac{|l\rangle\langle l|}{\mathrm{i}\tilde{\omega}_m - \epsilon_l\tau_l - \Sigma_l(\omega)\tau_l}. \tag{17}$$

We can define a complex self-energy, $\bar{\Sigma}_l(\omega) = \Sigma_l(\omega) - \mathrm{i}\tilde{\omega}_m$, where $\tilde{\omega}_m$ is the Matsubara frequency. As the single-particle states are disentangled, any mixedness in the state of the effective non-interacting metal can be attributed to a thermal scale $\tilde{\omega}_0 = 2\pi\beta^{-1}$. The Matsubara frequencies $\tilde{\omega}_m = \pi(2m+1)\beta^{-1}$ are defined as the mth harmonics of $\beta = 1/k_{\mathrm{B}}T$. Here we choose $m = 0$, i.e., $\tilde{\omega}_0 = \pi\beta^{-1}$ in order to find the largest temperature scale T upto which the poles will persist. By writing the imaginary part of the self energy as a Kramers–Kronig partner of the real self-energy, we obtain an equivalent temperature scale

$$\frac{\hbar}{\tau} = \frac{1}{\pi}\mathcal{P}\int_{-\infty}^{\infty} \frac{\Sigma_{j+1}(\bar{\omega})}{\bar{\omega} - \tilde{\omega}_0}\mathrm{d}\bar{\omega} \equiv \hbar\tilde{\omega}_0, \tag{18}$$

up to which the one-particle excitations can survive. A temperature scale for emergent gapped states of matter can be obtained similarly, and will be presented in section 6.

3.4. Fermi surface instabilities

As we will now see, the perfect nesting of the square FS (figure 2) indicates a putative instability of the FS via Umklapp back-scattering of an electronic pair. By summing over the elements of the transition matrix ($T(\Omega)$) for the Umklapp back-scattering processes we obtain the second order T-matrix element connecting electronic states assymetrically positioned about FS: one at distance Λ along $\hat{s}$ outside FS other at distance $-\Lambda - \delta$ along $\hat{s}'$ inside FS,

$$\lim_{\Omega\to 0} T^{(2)}_{\hat{s},\hat{s}'\to-\hat{s},-\hat{s}'}(\Omega) = \frac{1}{\mathrm{vol}^2}\lim_{\Omega\to 0}\sum_{\Delta\epsilon^{\mathrm{pair}}_{\Lambda,\delta}(\hat{s})}^{W} \frac{U_0^2}{\Omega - \Delta\epsilon^{pair}_{\Lambda,\delta}(\hat{s},\hat{s}')} = \frac{U_0^2}{(\mathrm{vol})^2 W}\ln\frac{W}{\Delta\epsilon^{\mathrm{pair}}_{\Lambda,\delta}(\hat{s},\hat{s}')}. \tag{19}$$

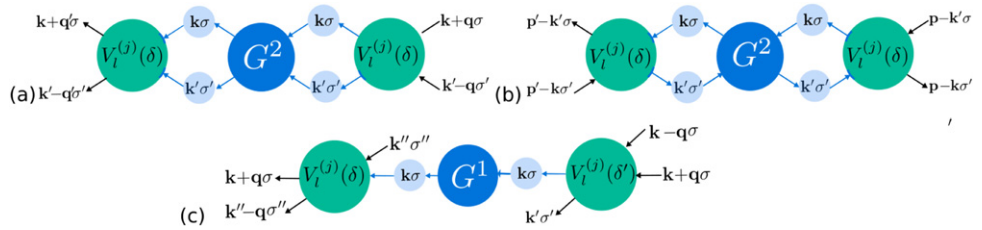

Figure 3. (a) and (b) Renormalization of the two particle scattering processes in the ee/hh, eh/he configurations respectively of the states $\mathbf{k}\sigma$, $\mathbf{k}'\sigma'$. Blue circle represents the intermediate ee or eh propagator. (c) Three particle processes generated from two particle scattering pairs $(\mathbf{k}\sigma, \mathbf{k}'\sigma')$, $(\mathbf{k}\sigma, \mathbf{k}''\sigma'')$ sharing a common state.

Here W is the bandwidth, vol is the system volume and $\Delta\epsilon^{\rm pair}_{\Lambda,\delta}(\hat{s},\hat{s}')$ is the net pair energy difference between the initial configuration i.e. a pair of electrons one above another below FS in the same quadrant and the scattered configuration i.e. a similar pair in the opposite quadrant. For pairs positioned symmetrically about the nodal vector $(\mathbf{Q}, \hat{s}' = T\hat{s} = (s_y, s_x))$ and around the FS $(\delta = 0)$ the difference in pair energy $\Delta\epsilon^{\rm pair}_{\Lambda,\delta} \to 0$ vanishes due to nesting in a square Fermi surface. Resultingly T-matrix has a leading order log divergence as $\lim_{\delta\to 0}\Delta\epsilon^{\rm pair}_{\Lambda,\delta} \to 0$. This indicates that the *resonant pairs* $(\delta = 0, \hat{s}' = T\hat{s})$ are more susceptible to instability compared to their assymetric counterparts, and will therefore dominate the physics of the Mott insulating state at low energies $(\Omega \to 0)$. As in the Kondo problem [58], such a log divergence in the T-matrix signals the need for an RG treatment of the FS instability.

A similar instability can be shown due to the *spin backscattering* process of opposite spin electron pairs (↑)-hole (↓) across the FS. It is important to note that the T-matrix elements are sensitive to Fermi surface geometry via dependence of $\Delta\epsilon^{\rm pair}_{\Lambda,\delta}(\hat{s},\hat{s}')$ on the normal $\hat{s}$ to the FS. This results in *electronic differentiation*: a range of quantum fluctuation scales associated with the instabilities across the FS (i.e., from the AN to the N), one for every $\hat{s}$ normal to Fermi surface. In the next section, we will treat these instabilities via the Hamiltonian renormalization group procedure equation (15), as well as identify the parent interacting metallic state of the Mott problem at 1/2-filling. We will also see that electronic differentiation leads to the nodal-antinodal dichotomy at the heart of the pseudogap phenomenon observed in doped Mott insulators [59–61].

3.5. RG flow equations for longitudinal and tangential scattering processes

In keeping with the discussions in the earlier section, we treat the Fermi surface instabilities arising from the two-particle scattering processes via the unitary operator based Hamiltonian RG formalism. Starting from the form of the unitary RG flow equation equation (15) we can obtain the RG flow equation for the two and three particle scattering vertices. Below we describe the steps leading to the RG flow equations.

In the figures 3(a) and (b) we depict the primary renormalization group contributions to the two particle vertices where the intermediate high energy state is a pair of electrons or an electron–hole pair respectively. Figure 3(c) depicts mixing between the various electron–electron and electron–hole scattering terms leading to three-particle scattering vertices. This is an outcome of the non-commutativity between the composite electron creation operator $(1-\hat{n}_{\mathbf{k}\sigma})c^\dagger_{\mathbf{k}'\sigma'}$ and the ee/eh pseudospin pair operators [62] $c^\dagger_{\mathbf{k}\sigma}c^\dagger_{\mathbf{k}'\sigma'}$ and $c^\dagger_{\mathbf{k}\sigma}c_{\mathbf{k}'\sigma'}$.

In order to incorporate the effect of off-diagonal three particle scattering vertices into the two particle vertices we perform a ω-dependent rotation, $\tan^{-1}\left(\sqrt{\frac{1-p}{p}}\right)$, in the space of the electron/hole configurations of $(\mathbf{k}', -\sigma) = (j, l')$, where $\mathbf{k}' = \mathbf{k}_{-\Lambda_j+\delta,T\hat{s}}$.

$$
\begin{aligned}
|\Uparrow\rangle &:= |1_{\mathbf{k}\sigma}\psi_{\mathbf{k}'-\sigma}\rangle = \sqrt{p}|1_{\mathbf{k}\sigma}1_{\mathbf{k}'-\sigma}\rangle + \sqrt{1-p}|1_{\mathbf{k}\sigma}0_{\mathbf{k}'-\sigma}\rangle,\\
|\Downarrow\rangle &:= |0_{\mathbf{k}\sigma}\psi^\perp_{\mathbf{k}'-\sigma}\rangle = \sqrt{1-p}|1_{\mathbf{k}\sigma}0_{\mathbf{k}'-\sigma}\rangle - \sqrt{p}|0_{\mathbf{k}\sigma}0_{\mathbf{k}'-\sigma}\rangle\,.
\end{aligned}
\tag{20}
$$

The state $|\mathbf{k}_{-\Lambda_j,T\hat{s}}\rangle$ is the reflected partner of the state $|\mathbf{k}_{\Lambda_j,\hat{s}}\rangle$ about the nodal direction N and constitutes a resonant pair. The momentum off-resonance δ in wavevector $\mathbf{k}' = \mathbf{k}_{-\Lambda_j+\delta,T\hat{s}}$ accounts for the asymmetric location of the state about the N direction. By projecting the operator RG flow equations for the forward and backward scattering vertices (A) in the spin/charge hybridized configurations $|\Uparrow\rangle$ and $|\Downarrow\rangle$ we obtain the coupling RG equations for the charge $((V_c/K_c)^{(j)}_l)$ and spin $((V_s/K_s)^{(j)}_l)$ type scattering

vertices ($p_+ = p = 1 - p_-$)

$$\frac{\Delta V^{(j)}_{\mathrm{c/s},l}(\delta)}{\Delta \log \frac{\Lambda_j}{\Lambda_0}} = \pm \frac{p_\pm (V^{(j)}_{\mathrm{c/s},l}(\delta))^2}{\mathrm{e}^{\mathrm{i}\gamma_l^{\Downarrow}} |G^{p,\Downarrow}_{j,l}|^{-1} - \frac{V^{(j)}_{p,l}(\delta)}{4}}, \quad \frac{\Delta K^{(j)}_{\mathrm{c/s},l}(\delta)}{\Delta \log \frac{\Lambda_j}{\Lambda_0}} = \pm \frac{p_\pm (K^{(j)}_{\mathrm{c/s},l}(\delta))^2}{\mathrm{e}^{\mathrm{i}\gamma_l^{\Uparrow}} |G^{p,\Uparrow}_{j,l}|^{-1} - \frac{K^{(j)}_{p,l}(\delta)}{4}}, \tag{21}$$

where $V^{(j)}_{p,l} = p_+ V^{(j)}_{\mathrm{c},l} - p_- V^{(j)}_{\mathrm{s},l}$ and $K^{(j)}_{p,l} = p_+ K^{(j)}_{\mathrm{c},l} - p_- K^{(j)}_{\mathrm{s},l}$. The Green's function $[G^{p,\Uparrow}_{j,l}]^{-1}$ is defined as

$$[G^{p,\Uparrow}_{j,l}]^{-1} = \left[\omega - p_+ \left(\frac{\epsilon_{j,l} + \epsilon_{j,l'}}{2} - \Delta\mu_{\mathrm{eff}}\right) - p_- \frac{\epsilon_{j,l} - \epsilon_{j,l'}}{2}\right]^{-1} \tag{22}$$

where a special value for p is chosen such that $G^{p,\Uparrow}_{j,l}$ is maximized,

$$p := p' \text{ s.t. } G^{p,\Uparrow}_{j,l} = \max_{0<p'<1} G^{p',\Uparrow}_{j,l} \tag{23}$$

and the electronic dispersion $\epsilon_{j,l'}$ in the definition of $G^{p,\Uparrow}_{j,l}$ is for the state $|(j,l')\rangle = |\mathbf{k}_{-\Lambda_j+\delta,\tilde{s}'}, -\sigma\rangle$. The Green's function $[G^{p,\Downarrow}_{j,l}]^{-1} = -[G^{p,\Uparrow}_{j,l}]^{-1}$ accounts for the poles of the orthogonal state $\Downarrow$. This special value in turn causes the maximization of the 2-particle vertex RG flows, ensuring their domination over the 3-particle off-diagonal vertex RG flows. Further, $\gamma^{(\Uparrow,\Downarrow)}_{\hat{s}}(\omega) = \mathrm{e}^{\mathrm{i}\pi(N_l^{\Uparrow,\Downarrow}(\omega)+1)}$ is the topological phase of the Green's function equation (22) with the topological invariant [63] $N_l^{\Uparrow,\Downarrow}(\omega) = \oint \mathrm{d}z [\mathcal{G}^{(j,l)}_{\Uparrow/\Downarrow}]^{-1} \partial_z \mathcal{G}^{(j,l)}_{\Uparrow/\Downarrow}$ where $[\mathcal{G}^{(j,l)}_{\Uparrow/\Downarrow}]^{-1} = z - [\hat{G}^{(j,l)}_{p,(\Uparrow/\Downarrow)}]^{-1}$. These topological invariants are constrained by the relation $N_l^{\Uparrow}(\omega) + N_l^{\Downarrow}(\omega) = 1$, such that an RG relevant forward scattering coupling implies an irrelevant backward scattering coupling. By integrating the RG equation (21), we obtain the RG invariant (C)

$$C = [pV^{(j)}_{\mathrm{s},l}(\delta)]^{-1} + [(1-p)V^{(j)}_{\mathrm{c},l}(\delta)]^{-1} = [pK^{(j)}_{\mathrm{s},l}(\delta)]^{-1} + [(1-p)K^{(j)}_{\mathrm{c},l}(\delta)]^{-1}. \tag{24}$$

In the Hubbard model (equation (1)), the bare values of various couplings are: $V^{(N)}_{\mathrm{s},l} = V^{(N)}_{\mathrm{c},l} = K^{(N)}_{\mathrm{s},l} = V^{(N)}_{\mathrm{c},l} = \bar{U}_0$, therefore $C^{-1} = p(1-p)\bar{U}_0$.

For tangential scattering processes (vertices represented by $L^{(j)}$), the intermediate state configuration necessarily involves electronic states on the entire isogeometric curve, i.e., the various many-body configurations obtained for a collective pseudospin angular momentum operator $L^z_j = 2^{-1}\sum_l (\hat{n}_{j,l} + \hat{n}_{j,l'} - 1)$. The scattering configuration are generated by collective pairwise electron raising/lowering operators $L^+_j = \sum_l c^\dagger_{j,l} c^\dagger_{j,l'}$ and L^-_j operators. The tangential scattering processes can involve the following class of intermediate state configurations,

$$|L_j = N_j + \frac{1}{2}, L^z_j = m + \frac{1}{2}\rangle = \sum_{m_1 = m+1-N_j}^{N_j} C^{j,m}_{m_1} \left|\frac{N_j}{2}, m_1\right\rangle \otimes \left|\frac{N_j+1}{2}, m - \frac{1}{2} - m_1\right\rangle, \tag{25}$$

where the quantum number m is related to the no. of electrons $N_j - m$ on the isogeometric curve. The above state has been represented in the tensor product space of two collective pseudospins $\mathbf{L}_j = \mathbf{L}_{1j} + \mathbf{L}_{2j}$, where $\mathbf{L}_{1j}$ is the net pseudospin vector made of $N_j + 1$ pseudospins and $\mathbf{L}_{2j}$ is made of N_j pseudospsins. The isogeometric curve constitutes $2N_j + 1$ pseudospins, N_j pseudospins in each of the two stretches $\left[(\pi, 0), \left(\frac{\pi}{2}, \frac{\pi}{2}\right)\right]$, $\left[\left(\frac{\pi}{2}, \frac{\pi}{2}\right), (0, \pi)\right]$ and 1 pseudospin along the nodal $N = \left(\frac{\pi}{2}, \frac{\pi}{2}\right)$ direction. In this Schmidt decomposition the Clebch Gordon coefficients $C^{j,m}_{m_1}$ are the Schmidt coefficients and the Schmidt rank [64] is $2N_j - m - 1$. These states are coupled by tangential scattering, such that the lower the magnitude of $|m|$, the higher is Schmidt rank; thus, for $m = 0$, the state $|L^z_j = \frac{1}{2}\rangle$ has the highest entanglement content.

The RG flow equation of the tangential scattering vertices can be found from the operator RG equation in A for the configuration given above in equation (25)

$$\Delta L^{(j)} = \frac{(N_j + m)(N_j - m + 1)(L^{(j)})^2}{\omega + Wsgn(\Delta\mu_{\mathrm{eff}}) + \tilde{\epsilon}^c_{j,\mathrm{avg}} - \frac{1}{4}L^{(j)}}, \tag{26}$$

where $\tilde{\epsilon}^c_{j,\mathrm{avg}} = N_j^{-1}\sum_l (\epsilon_{j,l} + \epsilon_{j,l'} - 2\Delta\mu_{\mathrm{eff}})$ is the average kinetic energy of the electrons on the high-energy isogeometric curve, and we have $\Lambda_j = \Lambda_0 \exp(-j)$ and $\Lambda_{j-1} = \Lambda_0 \exp(-(j-1))$, such that $\Delta \log \frac{\Lambda_j}{\Lambda_0} = 1$. The eigenvalues of L^2_j and L^{z2}_j are $= N_j(N_j+1)$ and m^2 respectively. We observe that the highly entangled $m = 0$ configuration maximizes the RG flow rate in equation (26). This indicates that due to the rich entanglement structure of the state with $m = 0$, the breaking of an electronic configuration with off-resonance pairs is unfavourable under RG. The value of the fluctuation operator scale ω is given by

$\omega + Wsgn(\Delta\mu_{\rm eff})$, where $W = 8t$ is the single-particle bandwidth. This can be argued as follows. For $\Delta\mu = 0$, beyond a minimum value of $\Delta\mu_{\rm eff}^{\rm min} = -W$, the tight-binding band has only holes with a Fermi surface shifted to the BZ centre $\mathbf{k} = (0, 0)$. As the low energy off-diagonal tangential scattering processes ($L^{(j)}(\delta)$) cause fluctuations of the minimum hole energy $E_{\rm hole}^{\rm min} = -(W/2) \times 2 = -\Delta\mu_{\rm eff}^{\rm min}$, the correct energy scale for quantum fluctuations is now given by $\omega + Wsgn(\Delta\mu_{\rm eff})$.

Gapless parts of the FS neighbourhood are characterised by back-scattering being RG irrelevant, but with forward scattering. The low lying excitations on such gapless stretches of the FS are strongly influenced by the RG flow equations of the three-particle scattering vertex operator (equation (A.8)) resulting out of forward scattering vertices. In the RG procedure the high energy states are chosen in a spin charge mixed configuration leading to the coupling flow equation for the three-particle scattering vertices as

$$\Delta R^{(j)}_{\hat{s},\delta\delta'} = \frac{V_l^{(j)}(\delta)V_l^{(j)}(\delta')}{\omega - \epsilon_{j,l}} + \frac{K_l^{(j)}(\delta)K_l^{(j)}(\delta')}{\omega - \epsilon_{j,l}} + \frac{R^{(j)}_{l,\delta\delta''}R^{(j)}_{l,\delta''\delta'}}{\left[G_{j,l,3}\right]^{-1} + \frac{1}{8}R^{(j)}_{l,\delta''}},$$
$$\left[G_{j,l,3}\right]^{-1} = p\left(\frac{\epsilon_{j,l} + \epsilon_{j,l'}}{2} - \Delta\mu_{eff}\right) + (1-p)\frac{\epsilon_{j,l} - \epsilon_{j,l'}}{2} - \omega. \tag{27}$$

Note that, once again, $\Lambda_j = \Lambda_0\exp(-j)$ and $\Lambda_{j-1} = \Lambda_0\exp(-(j-1))$, such that $\Delta\ \log\ \frac{\Lambda_j}{\Lambda_0} = 1$. It is easily seen that the choice of $\Lambda' = 0$, together with the optimal choice of the mixing parameter p (as made earlier in equation (21)) made in equation (A.8), maximises the 2 electron–1 hole (2e–1h) contribution to the above RG equation.

We now mention some other salient features of this RG formulation. First, the effective Hamiltonian at a given RG step can be formulated, with contributions from longitudinal (forward and backscattering, equation (21)), tangential (equation (26)) and three-particle diagonal and off-diagonal scattering vertices (equation (27)). The detailed form of the effective Hamiltonian is shown in appendix B. Next, the configuration energy for an mixed e-h/e-e intermediate pair is minimum for *resonant pairs* ($\delta = 0$) due to nesting geometry of the Fermi surface (see section 3.4). This leads to the propagator for $\delta = 0$ resonant pairs ($|\tilde{G}^{j,l}_{p,\Uparrow}|$,) having the highest magnitude in the RG equations for longitudinal scattering (equation (21)). In turn, this leads to the smallest denominators in these RG relations, ensuring that the resonant pairs dominate the RG flows for longitudinal scattering vertices.

Further, fixed points of the RG flows equations for longitudinal, tangential and three-particle vertices (equations (21), (26) and (27) respectively) are associated with the vanishing of their respective denominators: attaining a stable fixed point is related to the vanishing of quantum fluctuations such that no further decoupling of states can be carried out under the RG transformations (see equation (13)) [56]. Given that the resonant pairs dominate the RG flows, the spectral weight (characterised by the final distance from the FS, $\Lambda^*(\delta, \hat{s}, \omega)$) is also the highest at an RG fixed point for such pairs.

We find the dominant contributions to the RG equation for the 1 electron self energy comes from the backscattering ($K_l^{(j)}(\delta)$) and the three particle scattering ($R^{(j)}$) vertices,

$$\Delta\Sigma^{(j)}_{\Lambda\hat{s}} = \frac{K_l^{(j)}(\delta)K_l^{(j)}(\delta')}{\omega - \epsilon_{j,l} + \frac{1}{2}\epsilon_{j,l'} + \Sigma^{(j)}_{\Lambda_j\hat{s}}} + \sum_{\Lambda<\Lambda_j}\frac{(R_X^{(j)})^2}{\bar{\omega} - \frac{1}{2}\epsilon^c_{j,l} + \frac{1}{8}R_D^{(j)}}, \tag{28}$$

where $R_X^{(j)} = R^{(j)}_{l\delta\delta'}$, $R_D^{(j)} = R^{(j)}_{l\delta}$, and $\Lambda_j = \Lambda_0\exp(-j)$ and $\Lambda_{j-1} = \Lambda_0\exp(-(j-1))$, such that $\Delta\ \log\ \frac{\Lambda_j}{\Lambda_0} = 1$. We note that the Green's function of the first term involve a 2e–1h composite [65] of states: $|\mathbf{k}_{\Lambda_j\hat{s}}\uparrow\rangle$, $|\mathbf{k}_{\Lambda_j\hat{s}}\downarrow\rangle$ and $|\mathbf{k}_{-\Lambda_j T\hat{s}\downarrow}\rangle$, where the first two refer to the electron occupied states above the Fermi surface and the last to a hole state located below the Fermi surface. Similarly, $\epsilon^c_{j,l} = \epsilon_{j,l} + \epsilon_{j,l'}$ appearing in the denominator of the second term is the dispersion for a three electrons and two hole composite, of which one electron and two holes reside at Fermi energy. We now show that the quantum fluctuation scale ω determines the nature of the self energy RG equation. At scales $4 - \omega > 4 - \omega_{\rm PG}$, the backscattering vertex ($K^{(j)}$) is RG irrelevant everywhere on the Fermi surface, resulting in the renormalization of Σ solely from the three-particle vertex. The fixed point neighbourhood can then be explored via a diagonal and off-diagonal two electron particle vertex with strengths R_D and R_X respectively. This will be discussed in a later section. Upon lowering $4 - \omega$ below $4 - \omega_{\rm ins}$, however, the backscattering vertex is dominant everywhere on the Fermi surface, leading to the self energy being renormalized predominantly by them.Given that the denominator of the first term is always positive, the RG flow of Σ is towards a strong coupling fixed point $\Sigma \to \infty$. This naturally leads to a zero in the 1 electron Green's function, and as we will see below, a gapping of the Fermi surface. In appendix A, we present a comparison of our results with those obtained from a weak-coupling functional RG approach.

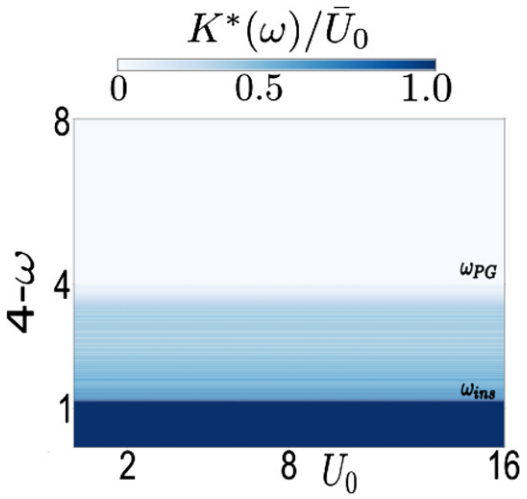

Figure 4. $T = 0$ Renormalisation group phase diagram at $1/2$-filling in the quantum fluctuation energyscale $(4 - \omega)$-bare repulsion (U_0) plane. Colourbar represents ratio of renormalized coupling to bare coupling $K^*/\bar{U}_0$. Transition from non-Fermi liquid (NFL, white) to Mott liquid (ML, dark blue) insulator is through a pseudogap (PG, shaded blue) for all $U_0 > 0$. $\omega_{\rm PG}$ and $\omega_{\rm ins}$ are energy scales for Lifshitz transitions that initiate and end the PG respectively. This phase diagram was obtained for a 1024×1024 sized momentum-space grid.

In this way, we have provided an RG-based justification for the backscattering T-matrix argument given earlier (equation (19)). Finally, the RG equations can be solved numerically in an iterative manner on a two-dimensional momentum-space grid, leading to fixed point values of various couplings, spectral weights and gaps. From these, we can draw an RG phase diagram, as well as compute several physical observables. In the following sections, we adopt this procedure in unveiling the physics of the $T = 0$ Mott–Hubbard transitions at $1/2$-filling.

4. Mott MIT at $1/2$-filling: the normal state

The $T = 0$ phase diagram obtained by integrating the RG equations set out in the previous section at $1/2$-filling ($\mu^0_{\rm eff} = 0$) is shown in figure 4. Prior to the detailed discussions that will follow, we outline the key aspects displayed in the RG phase diagram. First, an explanation of the axes: the y-axis represents the energy scale ω for quantum fluctuations where $0 \leqslant \frac{W}{2} - \omega \leqslant 8t$ and the x-axis represents the bare value of the on-site Hubbard coupling ranging from weak to strong coupling ($0 < U_0 \leqslant 16 = 2W$). A striking observation is that the Mott metal–insulator transition (MIT) involves the passage from a gapless metallic normal state at high ω to a gapped insulating Mott liquid (ML) groud state at low ω, but through a pseudogapped (PG) state of matter (at intermediate values of ω) arising from a differentiation of electrons based on the monotonic variation of their dispersion from linear in momentum at node (N) to quadratic at antinode (AN) [66, 67].

In order to obtain the phase diagram shown in figure 4, we have taken into account the RG flow of the forward ($V_l^{(j)}$), backward ($K_l^{(j)}$) and tangential ($L^{(j)}$) scattering vertices in the electron–electron (BCS) and electron–hole (ZS and ZS′)channels. In figures 5 and 6, we present the RG scale dependence of the $V_{{\rm c},l}^{(j)}$) and $K_{{\rm c},l}^{(j)}$ scattering vertices for four normal directions (two near N and two near AN) associated with the Fermi surface wave vectors $\mathbf{k}_{\rm F}$: $1 : -\left(\frac{\pi}{2}, \frac{\pi}{2}\right)$, $2 : -\left(\frac{\pi}{4}, \frac{3\pi}{4}\right)$, $3 : -\left(\frac{\pi}{8}, \frac{7\pi}{8}\right)$, $4 : -\left(\frac{\pi}{16}, \frac{15\pi}{16}\right)$. In figure 5, panel a and panel b represents the RG flow of the vertices at $\omega = -1$ (i.e., within the gapless non Fermi liquid (NFL) phase) and $\omega = 3$ [within the gappled Mott liquid (ML) phase] respectively. The left figure in panel a shows the RG irrelevant backscattering vertices $K_{{\rm c},l}^{(j)}$ in the electron–electron channel for the four normal directions, while the right figure of panel a shows RG relevant forward scattering vertices $V_{{\rm c},l}^{(j)}$ that stop at an intermediate coupling fixed point characterising the NFL. On the other hand, panel b shows the opposite behaviour, i.e., a relevant backscattering vertex that attains an intermediate coupling fixed point characterising the ML, and an RG irrelevant forward scattering vertex that vanishes along the RG flow.

Also, note that in the left figure in panel (b) of figure 5, the black curve (representing the backscattering vertex $K_{\rm c}$ close to antinodes $(\pi/16, 15\pi/16)$) has the highest magnitude; the value of $K_{\rm c}$ falls upon approaching the nodal direction. This dependence of the vertex RG flows on the direction normal to the Fermi surface arises from the different nature of the electronic dispersion spanning across the Fermi surface (i.e., from AN to N), and is observed in all the figures in figures 5 and 6. Panel (a) of figure 6 represents the

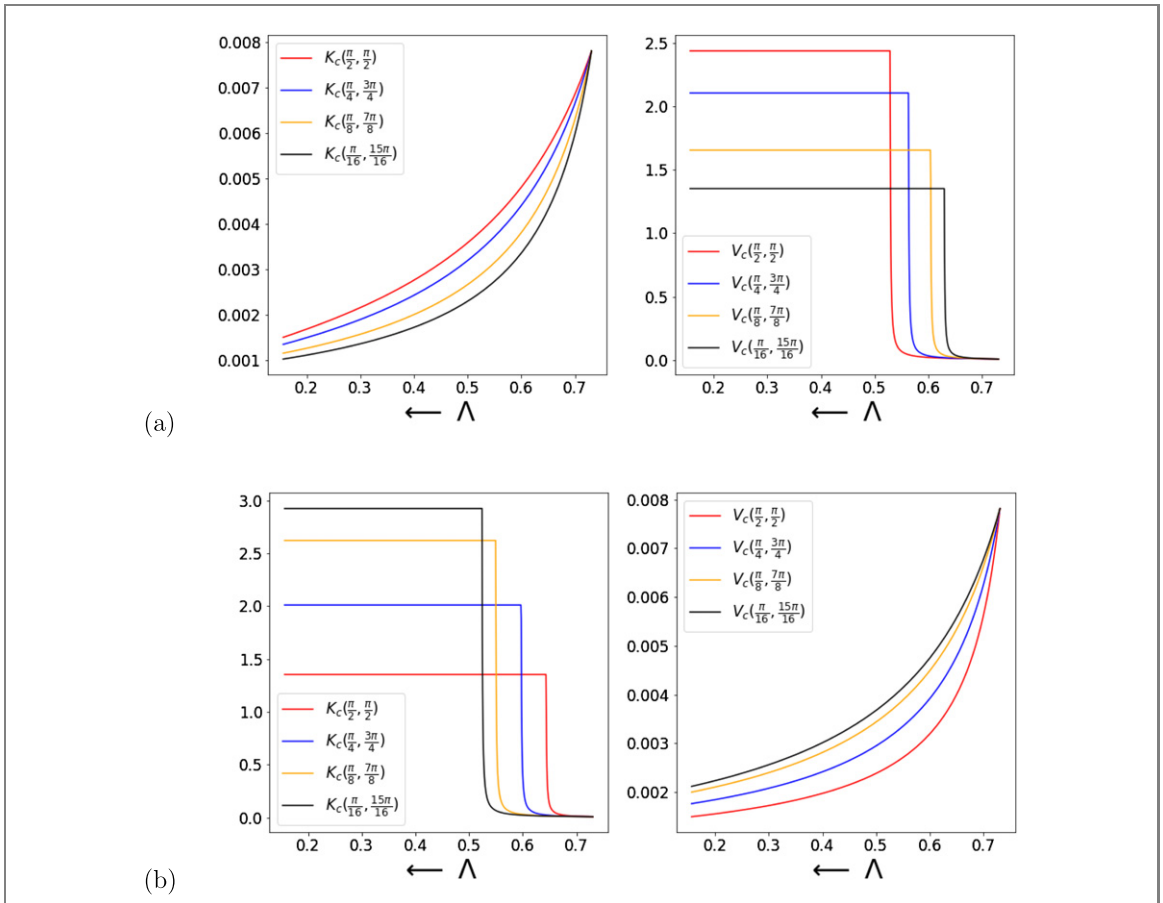

Figure 5. Plots of the RG flows for the forward (V_c) and backward (K_c) scattering couplings with scaling towards the Fermi surface (via decrease in the RG cutoff scale Λ) in the metallic [NFL, panel (a)] and insulating [ML, panel (b)] phases. Panel (a) represents the RG flow for the forward (right figure) and backward (left figure) scattering vertices describing the NFL phase at $\omega = -1$. Panel (b) represents the RG flow of the vertices in the ML phase at $\omega = 3$. Numerical simulations for the RG equations were performed on a 1024×1024 momentum space grid.

relevant and irrelevant vertices at the onset of the PG phase $\omega = 0.05 - \omega_{\rm PG}$. We observe that the NFL persist along the normal directions 1, 2, 3 (starting from N); however, along the antinodal direction 4, the NFL is replaced by the gapped Mott liquid phase. Panel (b) of figure 6, on the other hand, represents the vertices in the vicinity of the final transit from the PG phase into the Mott liquid phase ($\omega = 2.5$). Here, only the nodal direction retains the NFL, while all other directions show the gapped ML behaviour. This makes it evident the fluctuation scale ω play an important role in determining the relevant vertices and there associated fixed points. We note that similar observations on the role of a frequency scale on RG flows have also been made from recent functional RG calculations [32].

The PG phase is described by partial gap in the neighbourhood of AN, with a gapless stretch centred around N. The gapping process is initiated at the ANs as an FS topology-changing Lifshitz transition of the normal phase at fluctuation scale $\omega = \omega_{\rm PG} \equiv 0.034t$, and proceeds until the Ns are gapped out in a Mott liquid state via a second Lifshitz transition at $\omega = \omega_{\rm ins}$ (figure 7(b), video S1). Figure 7(b) represents a snapshot of the gapped and gapless parts of FS at $\omega = 2.5$. The cyan region (colorbar represents the fixed point backscattering coupling $\Delta = K^*(\Lambda, \hat{s})$ obtained from RG equations) $R_1 : \left[-\Lambda^*_{\hat{s}}, \Lambda^*_{\hat{s}}\right]$ for $\hat{s}$ between $[\hat{s}_{\pi,0}, \hat{s}_1]$ and $[\hat{s}_1, \hat{s}_{0,\pi}]$ represents the nonuniform window of width $2\Lambda^*_{\hat{s}}$ along the gapped part of Fermi surface. Region R_2 stretching along FS $[\hat{s}_{\rm N} - \delta\hat{s}, \hat{s}_{\rm N} + \delta\hat{s}]$ represents the gapless arc centred about the nodal direction: $2\delta\hat{s}$ is the length of the gapless stretch. The spectral function $A(\Lambda, \hat{s})$ in region R_2 is represented by the red to yellow colorbar. Region $R_3 : \left[-\Lambda_0, -\Lambda^*_{\hat{s}}\right)\big]$ and $\left[\Lambda^*_{\hat{s}}, \Lambda_0\right]$ represents the nonuniform quasiparticle spectral function $A(\Lambda, \hat{s})$ present outside the region R_1. Here Λ_0 is the bare momentum space cut-off scale. The inset shows the spectral function $A(E, \hat{s})$ along two normal directions, i.e., along the nodal direction $A(E, \hat{s}_{\rm N})$ in red, the antinodal $A(E, \hat{s}_{\rm AN})$ in blue, while the average spectral function $A(E)$ is shown in the black curve.

We develop the RG fixed point theory for the normal phase in this section. The next section is devoted to the PG phase and the Lifshitz transition leading to it. We complete our discussion for the Mott MIT at 1/2-filling by by focussing on the Mott liquid in detail in a subsequent section. It is also worth noting the

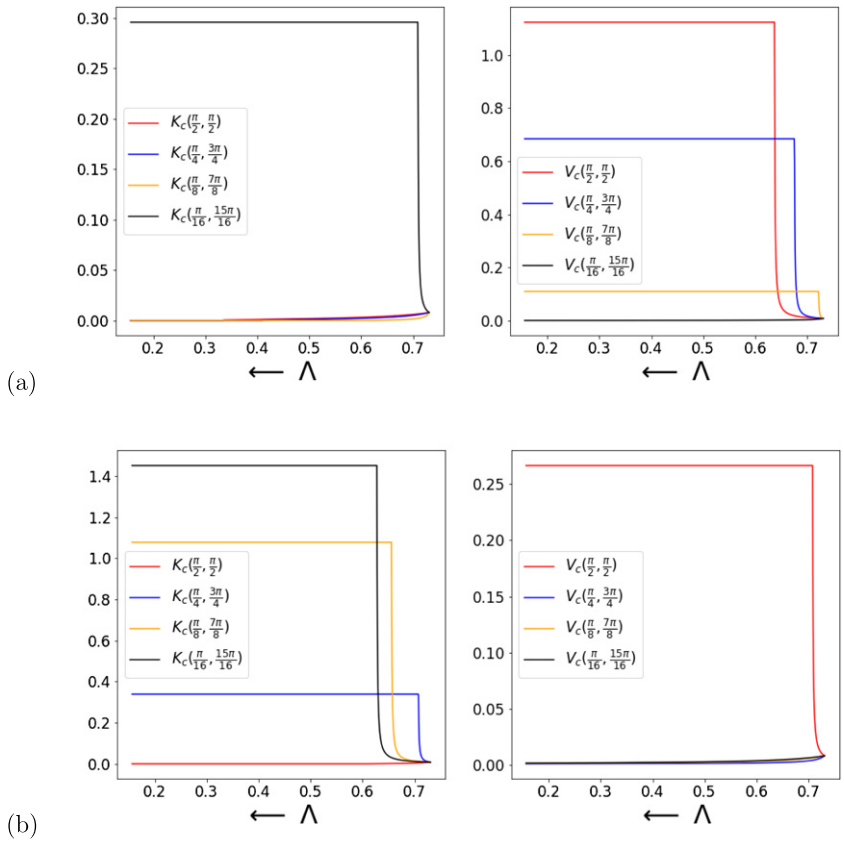

Figure 6. Plots of the RG flows for the forward (V_c) and backward (K_c) scattering couplings with scaling towards the Fermi surface (via decrease in the RG cutoff scale Λ) in the pseudogap (PG) phase. Panel (a) represents the RG flow for the forward (right figure) and backward (left figure) scattering vertices describing the onset of the PG phase at $\omega = 0.05$. Panel (b) represents the RG flow of the vertices in the vicinity of the transition $\omega = 2.5$ from the PG to ML phase. The numerical simulations for the RG equations were performed on a 1024×1024 momentum space grid.

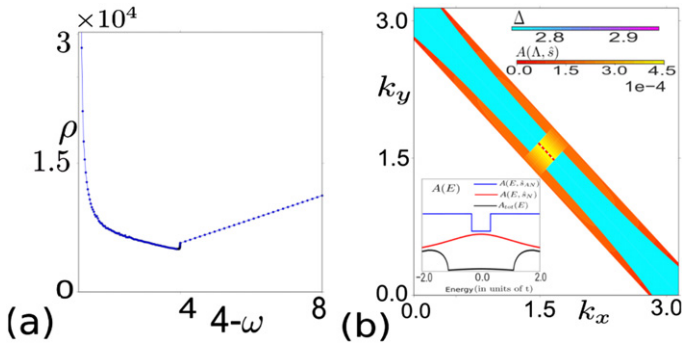

Figure 7. ((a) Linear variation of resistivity (ρ) with $\omega < \omega_{PG}$ in NFL crosses over through PG ($\omega_{PG} < \omega < \omega_{ins}$) into the ML (diverging ρ for $\omega > \omega_{ins}$). (b) $A(E)$ (colourbar: red to yellow) and Δ (magnitude of the backscattering vertex, $K^*(\Lambda, \hat{s})$, colourbar: cyan to violet) in first quadrant of BZ with changing $\omega = 2.5$. The dashed red line represents the remnant Fermi surface in the gapless stretch. Inset: quasiparticle (qp) spectral function ($A(E)$) for $\omega = 2.5$, showing NFL at N (red curve) and gap at AN (blue curve) and averaged over FS (A_{tot}, black curve). The resistivity plot in (a) and contour plot for Δ and $A(\Lambda, \hat{s})$ in (b) were obtained for a 1024×1024 sized momentum-space grid.

flatness of the phase boundaries: this indicates the absence of a critical $(U/t)_c$ for the metal–Mott insulator transition for the 1/2-filled Hubbard model on the 2D square lattice with only nearest neighbour hopping, and results from the perfectly nested FS [68, 69]. This is consistent with recent DΓA and quantum Monte Carlo simulations of the unfrustrated Hubbard model by Schäfer *et al* [22]. We anticipate the presence of a critical $(U/t)_c$ in the generalised Hubbard model with an additional (frustrating) next-nearest neighbour hopping, as has been demonstrated in dynamical mean-field theory (DMFT) studies [70, 71].

The U_0 independent gapping of the antinodes can be anticipated from the divergence of the second order T-matrix element equation (19) for both resonant ($\delta = 0$) as well as off-resonant ($\delta \neq 0$) pairs. This

results from the vanishing of the energy transfer at the antinodes $k_x, k_y = \pi, 0$ and $0, \pi$. at $\Omega = 0$ and the existence of van Hove singularities of the DOS at the antinodes. Thus, this event marks the onset energy scale of the pseudogap, $\omega_{\rm PG} = \frac{1}{2}(\epsilon_{\Lambda_0,\hat{s}_{\rm AN}} - \epsilon_{-\Lambda_0,T\hat{s}_{\rm AN}})$, where $\epsilon_{\Lambda_0,\hat{s}_{\rm AN}}$ is the energy of the electronic state along the antinodal direction residing at the bare cutoff scale Λ_0 outside FS. The energy of the partner hole state is $-\epsilon_{-\Lambda_0,T\hat{s}_{\rm AN}}$. On the other hand, along the nodal direction $k_x = k_y = \pi/2$, the energy transfer is $\Delta E = 4t\ \sin\frac{\Lambda}{\sqrt{2}}\left[\cos\frac{\delta}{\sqrt{2}} - 1\right] \neq 0$. This lowers considerably the gapping of the nodal points on the FS, and therefore the onset energy scale for the Mott insulator, $\omega_{\rm ins} = \frac{1}{2}(\epsilon_{\Lambda_0,\hat{s}_{\rm N}} - \epsilon_{-\Lambda_0,T\hat{s}_{\rm N}})$ where $\epsilon_{\Lambda_0,\hat{s}_{\rm N}}$ is the energy of the electronic state along the nodal direction residing at the bare cutoff scale Λ_0 outside FS. The energy of the partner hole state is $-\epsilon_{-\Lambda_0,T\hat{s}_{\rm N}}$. This is indicated by the fact that only the resonant ($\delta = 0$) scattering events along the nodal direction contribute to the T-matrix element in a divergent manner at $\Omega \to 0$ (equation (19)). Further, this divergence is again U_0 independent. These arguments show that the Fermi surface topology-changing events, i.e., the disconnection of the antinodes at $\omega_{\rm PG}$ and the vanishing of the nodal arcs at $\omega_{\rm ins}$, are both U_0 independent and are only related to the geometry of the underlying lattice. We note that the numerical investigations of references [22, 72] show that at finite temperatures, the Mott transition in the 2D Hubbard model is pre-empted and precluded by crossovers from a gapless metal to a quasi-antiferromagnetic insulator via a pseudogapped state of matter. The crossovers are dependent on the bare value of the Hubbard repulsion U, in contrast to our findings for the scales $\omega_{\rm PG}$ and $\omega_{\rm ins}$. As discussed above, these scales originate in the electron differentiation inherent in the tight binding problem, and are likely to possess corrections from two-particle correlations that have been neglected at present. Taking such corrections into account is important for resolving the discrepancy with the results of references [22, 72]. This limitation of our work deserves further investigation, and will be dealt with in a subsequent work.

4.1. Normal state for the Mott insulator

In charting the physics of the normal state from which the gapped Mott insulator arises, we will carry out the RG analysis using the two particle and three particle vertex scattering RG flow equations equations (21), (27). For this, we note that in the quantum fluctuation range $\frac{W}{2} < \frac{W}{2} - \omega < W$, from the RG eqns. Equation (21) all the backscattering vertices that destabilize the FS (equation (19)) are RG irrelevant while forward scattering vertices are RG relevant. This ensures the existence of metallic state topologically protected by global index $N_{\hat{s}}^{\Downarrow}(\omega) = 1\ \forall \hat{s}$.

Further, the tangential scattering coupling (whose flow equation is shown in equation (26)) is also found to be RG irrelevant, as the denominator is negative $\omega + \tilde{\epsilon}^{c}_{\Lambda_j,\rm avg} < 0$. Thus from the stable fixed points of the RG flow equations we obtain an effective Hamiltonian $H^* = H_1 + H_2$ in two parts: H_1 describes nature of the normal state near FS, H_2 describes the normal state away from FS. First we describe the physics of H_2,

$$H_2 = \sum_{j,l} \epsilon_{\Lambda_j\hat{s}}\hat{n}_{j,l} + \sum_{j,j',l} R^{(j)}_{l\delta}\hat{n}_{j,l}\hat{n}_{j,l'}(1 - \hat{n}_{j',l}) + \sum_{j,j',l} V^{(j)}_{l}(\delta)\hat{n}_{j,l}\hat{n}_{j,l'}. \tag{29}$$

The states $|j,l\rangle = |\mathbf{k}_{\Lambda_j\hat{s}}\sigma\rangle$, $|j,l'\rangle = |\mathbf{k}_{-\Lambda_j+\delta T\hat{s}}\sigma\rangle$, $|j',l\rangle = |\mathbf{k}_{\Lambda_{j'}\hat{s}}\sigma\rangle$. For the one particle dispersion $\epsilon_{\Lambda_j\hat{s}}$ and two particle correlation energy $V^{(j)}_{l\delta}$ the summation is restricted to $\Lambda_j > \Lambda^{**}_{\hat{s}}$, for every normal $\hat{s}$. The 2 particle 1 hole dispersion $R^{(j)}_{l\delta}$ is restricted to $\Lambda^{*}_{\hat{s}} > \Lambda_j > \Lambda^{**}_{\hat{s}}$. The momentum space scales $\Lambda^{*}_{\hat{s}}, \Lambda^{**}_{\hat{s}}$ generated by the RG scheme will be described below. As the RG proceeds by decoupling states far from FS we reach an effective theory described by forward scattering processes only, $K^{(j*)}_{{\rm c},l}(\delta) = K^{(j*)}_{{\rm s},l}(\delta) = 0$ and $V^{(j*)}_{{\rm c},l}(\delta) = \frac{1}{2}(\epsilon_{j*,l} + \epsilon_{j*,l'} - \omega)$. Scattering processes associated with different off-resonant pairs δ is restricted to different momentum space widths Λ^{*}_{δ} around FS. In this way we obtain the scale $\Lambda^{*}_{\hat{s}} = \max_{\delta}\Lambda^{*}_{\delta,\hat{s}}$ that is the largest among all the momentum space widths. Further the scale $\Lambda^{*}_{\hat{s}}$ is anistropic in momentum space manifested by the C_4 lattice geometry. Beyond the $\Lambda^{*}_{\hat{s}}$ window only two particle number diagonal interactions $V^{(j*)}_{{\rm c},l}(\delta)$ persist in momentum space describing a Fermi liquid-like gapless metallic state of matter. This Fermi liquid is positioned farthest away from the non-interacting FS in energy as well as in k-space.

The non-commutativity between different forward scattering terms within the window $\Lambda^{*}_{\hat{s}}$, leads to an effective three-particle (2e–1h) scattering term following equation (27) (shown in figure 3). By performing a second step RG at fluctuation energy scale $\bar{\omega} = \max_{\delta,\hat{s}} 2^{-1}(\epsilon_{j^*,l} + \epsilon_{j^*,l'})$ in the vicinity of the momentum space window $\Lambda^{*}_{\hat{s}}$ we find that the forward scattering couplings are RG irrelevant and flow towards vanishing coupling, $V^{(j**)}_{{\rm c},l}(\delta) = 0$. On the other hand, we find that the flow of the 2e–1h off-diagonal scattering terms generated from the forward scattering processes (first term in equation (27)) are initially RG relevant. Given that backscattering vertices are RG irrelevant so the 2nd term in equation (27) vanishes. As the 2e–1h scattering processes becomes bigger in magnitude, the third term in equation (27) eventually

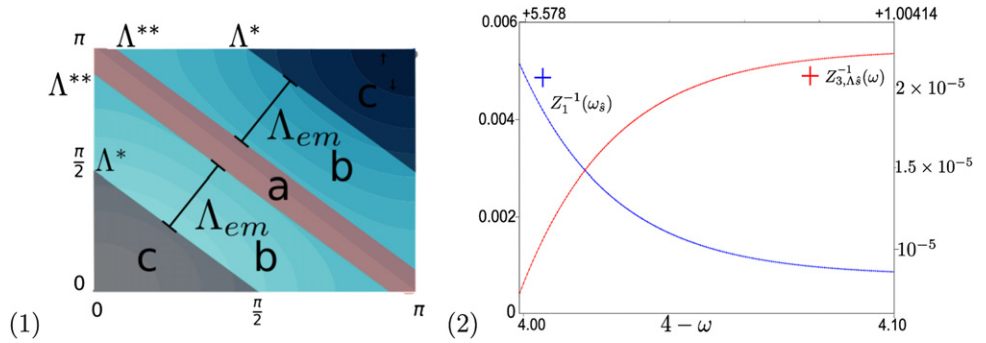

Figure 8. (1) Momentum-space map partitioned into regions with different Hamiltonian structures for the normal state. (a) represents the marginal Fermi liquid (MFL), (b) represents a correlated Fermi liquid, i.e., containing both MFL and Fermi liquid (FL), (c) represents an FL. (2) Inverse quasiparticle residue averaged over a gapless connected Fermi surface $Z_{\rm avg}^{-1}$ at energies above the entry into the pseudogap phase shows a logarithmic growth as $4-\omega$ is lowered towards the Fermi energy ($\omega \to 4-$). Vanishing of the quasiparticle residue (as the Fermi energy is approached) is an important characteristic of the destruction of the Fermi liquid. Instead, $Z_{3,\Lambda\hat{s}}^{-1}$ gradually rises to unity near the Fermi energy.

cuts off their growth to the fixed point,

$$\frac{R^*_{l\delta}}{8} = \bar{\omega} - \frac{1}{2}(\epsilon_{j**,l} + \epsilon_{j**,l'}), \quad V^{**}_{l\delta} = 0\,, \tag{30}$$

where $(j**, l) = (\mathbf{k}_{\Lambda^{**}\hat{s}}\sigma)$. This leads to the generation of a second momentum space scale $\Lambda^{**}_{\hat{s}}$ below which the Fermi liquid is absent. Thus, the momentum space region $\Lambda^{*}_{\hat{s}} > \Lambda > \Lambda^{**}_{\hat{s}}$ constitutes an admixture of the two particle and three particle number diagonal terms. This gradual crossover leads to a very different gapless metallic state of matter in the immediate neighbourhood of the FS described by

$$H_1 = \sum_{j,l} \epsilon_{j,l}\hat{n}_{j,l} + \sum_{j,j',l} R^*_{l\delta}\hat{n}_{j,l}\hat{n}_{j,l'}(1-\hat{n}_{j',l}). \tag{31}$$

The first and second terms in the expression have their summations limited to j and j', such that $\Lambda_j, \Lambda_{j'} < \Lambda^{**}_{\hat{s}}$ for the various normal $\hat{s}$ to FS. Thus, the intermediate window involves a gradual crossover from a Fermi liquid to another metallic state of matter (see figure 8(a)) which we characterise below.

4.2. Marginal Fermi liquid in the IR

We will now see that the gapless state of matter lying at lowest energies possesses properties ascribed phenomenologically to the marginal Fermi liquid [73]. Of primary importance is the renormalisation of the 1-particle self-energy arising from three particle scattering terms in the neighbourhood of the fixed point (equation (30)). From the discussion following equation (28), the dominant contribution to the one particle self energy RG flow in the regime $4-\omega > 4-\omega_{\rm PG}$ is

$$\begin{aligned}
\Delta\Sigma^{{\rm Re},*}_{\Lambda,\hat{s}}(\bar{\omega}) &= N(\Lambda_j,\hat{s})\frac{(R^{(j)}_X)^2}{R^{(j)}_D}\int_{0,\delta\to 0}^{\Lambda_j}\frac{{\rm d}\epsilon_{\Lambda_j}}{\bar{\omega} - \frac{1}{2}\epsilon^c_{j,l} + \frac{1}{8}R^{(j)}_D} \\
&= N(\Lambda^{**},\hat{s})\frac{(R^{*}_X)^2}{R^{*}_D}\,\ln\frac{\bar{\omega}}{\bar{\omega} - \frac{1}{2}\epsilon^c_{j**,l} + \frac{1}{4}R^{**}_D} \\
&= N(\Lambda^{**},\hat{s})\left(\bar{\omega} - \frac{1}{2}\epsilon_{j**,l}\right)\ln\left|\frac{8\bar{\omega}}{\bar{\omega} - \frac{1}{2}\epsilon_{j**,l}}\right|\,,
\end{aligned} \tag{32}$$

where $R^*_X = R^{(j**)}_{l\delta\delta'}$, $R^*_D = R^{(j**)}_{l\delta}$ and $\epsilon^c_{j,l} = \epsilon_{j,l} + \epsilon_{j,l'}$ is the dispersion for an electronic pair. Note that we have replaced the summation on the right-hand side of equation (28) by an integral. We have introduced the total number of states within window Λ^{**} along a given $\hat{s}$ as $N(\Lambda^{**},\hat{s})$. In the last step we have used the RG invariant relation $C = R^{(j)}_X - R^{(j)}_D = 0$ resulting from the RG equation $\Delta R^{(j)}_X = \Delta R^{(j)}_D$ and used the fixed point value of $R^{(j**)}_{l\delta}$ equation (30). As the self energy renormalization has a branch-cut log singularity at the FS, we may approximate $\Sigma^{{\rm Re},(j)}_{\mathbf{k}_{\Lambda\hat{s}}}(\omega) \approx \Delta\Sigma^{{\rm Re},(j)}_{\mathbf{k}_{\Lambda\hat{s}}}(\omega) + O(\omega)$. From these relations, we obtain the self energy Σ and the quasiparticle residue Z_1 as

$$\Sigma(\tilde{\omega}_{\hat{s}}) = \tilde{\omega}_{\hat{s}}\,\ln\left|\frac{N^*(\hat{s},\omega)\bar{\omega}}{\tilde{\omega}_{\hat{s}}}\right|, \quad Z_1(\tilde{\omega}_s) = \frac{1}{2 - \ln\left|\frac{\tilde{\omega}_{\hat{s}}}{N(\hat{s},\Lambda^{**})\bar{\omega}}\right|}, \tag{33}$$

where $\tilde{\omega}_{\hat{s}} = N^*(\hat{s},\omega)\left(\bar{\omega} - \frac{1}{2}\epsilon_{\Lambda^{**},\hat{s}}\right)$. The quasiparticle residue $Z_1(\tilde{\omega}_s)$ vanishes as $\tilde{\omega}_{\hat{s}} \to 0$, indicating breakdown of Landau's quasiparticle picture. These well-known expressions for the marginal Fermi liquid have been proposed on phenomenological grounds towards understanding the strange metal phase encountered in the hole-doped cuprates [73]. While Σ has the same structure as proposed in [73], it is worth noting that the marginal Fermi liquid we find arises from singular forward scattering normal to the Fermi surface.

The imaginary part of the self energy can be computed from the real part of the self energy using the Kramers–Kronig relations

$$\Sigma^{\mathrm{Im},(j)}_{\Lambda_j,\hat{s}}(\bar{\omega}_{\hat{s}}) = \frac{1}{\pi}\mathcal{P}\int_{-\infty}^{\infty}\frac{\Sigma^{\mathrm{Re},(j)}_{\Lambda_j,\hat{s}}(\omega)}{\omega - \tilde{\omega}_{\hat{s}}} = \tilde{\omega}_{\hat{s}}\,. \tag{34}$$

From here, we obtain the quasiparticle lifetime as $\tau = 2\pi\tilde{\omega}_{\hat{s}}^{-1}$, in keeping with the proposed relation for the marginal Fermi liquid. Further using the equivalence relation between the quantum fluctuations assisted broadening $\tilde{\omega}_{\hat{s}}$ and thermal broadening (equation (18)), we can obtain the largest temperature scale (T) upto which the single particle description is well defined

$$k_{\mathrm{B}}T = \hbar\max_{\hat{s}}\tilde{\omega}_{\hat{s}}\,. \tag{35}$$

The inverse lifetime τ^{-1} is thus associated with a linear-in-T Drude resistivity, $\rho \propto T$, arising from the excitations of the gapless Fermi surface. As $\omega \to 0$ and $\Lambda^{**} \to 0$, the 2e–1h dispersion equation (30) vanishes $R^*_{l\delta} \to 0$ therefore the two-electron 1 hole residue $Z_3 \to 1$, making the composite degree of freedom well defined. This is exhibited by the fixed point Hamiltonian equation (31). The spectral weights/residues for 1e ($Z_1(\omega_{\hat{s}})$) and 2e–1h composite ($Z_{3,\Lambda\hat{s}}(\omega) \to 1$) are computed numerically from the above Green's functions, and shown in figure 8(b). The figure shows that as the FS is approached ($\omega \to 4$), a vanishing $Z_1(\omega_{\hat{s}})$ is compensated by a $Z_{3,\Lambda\hat{s}} \to 1$. In the following sections, we describe the destablization of the marginal Fermi liquid metallic state leading to various other exotic phases at lower fluctuation scales.

5. RG flow through the pseudogap

In the energy range $\frac{W}{2} - \omega_{\mathrm{PG}} < \frac{W}{2} - \omega > \frac{W}{2} - \omega_{\mathrm{ins}}$, the pseudogap is initiated in the form of an FS topology-changing Lifshitz transition that disconnects the connected FS via a gaping of the antinodes for $\omega < \omega_{\mathrm{PG}} \equiv 0$, and proceeds until the nodes are gapped via a second Lifshitz transition at $\omega = \omega_{\mathrm{ins}}$ (figure 1(d), video S1). This is an outcome of electronic differentiation arising out of a variation of the electronic dispersion from quadratic to linear along the Fermi surface [66] which influences the ee or eh paring energy. While the resistivity shows a linear behaviour with $W/2 - \omega$ in the metallic phase (i.e., in the range $\omega_{\mathrm{PG}} \leqslant W/2 - \omega \leqslant W$), in the PG phase (figure 7(a), the resistivity shows a crossover into an insulator phase, i.e., an increase with lowering $\frac{W}{2} - \omega$ beyond $\omega = \omega_{\mathrm{PG}}$. At a given fluctuation scale within the above given energy range , the fixed point Hamiltonian of the gapped parts of the FS is described by *resonant pairs* as they condensed at lowest energies carrying the highest spectral weight,

$$\hat{H}^*(\omega) = \sum_{\hat{s}} N^{\Uparrow}_{\hat{s}}(\omega)\left(K^*_{c,\hat{s}}(\omega)\mathbf{A}_{*,\hat{s}}\cdot\mathbf{A}_{*,-\hat{s}} - K^*_{s,\hat{s}}(\omega)\mathbf{S}_{*,\hat{s}}\cdot\mathbf{S}_{*,-\hat{s}}\right) + \sum_{\hat{s}} N^{\Downarrow}_{\hat{s}}(\omega)H^*(\omega,\hat{s}), \tag{36}$$

where the charge ($\mathbf{A}$) and spin ($\mathbf{S}$) are the net pseudospin operator, defined as

$$\mathbf{A}_{*,\hat{s}} = \sum_{\Lambda<\Lambda^*_{\hat{s}\omega}}\mathbf{A}_{\Lambda,\hat{s}},\quad \mathbf{S}_{*,\hat{s}} = \sum_{\Lambda<\Lambda^*_{\hat{s}\omega}}\mathbf{S}_{\Lambda,\hat{s}},\quad \mathbf{A}_{\Lambda,\hat{s}} = f^{c;\dagger}_{\Lambda,\hat{s}}\frac{\sigma}{2}f^{c}_{\Lambda,\hat{s}},\quad \mathbf{S}_{\Lambda,\hat{s}} = f^{s;\dagger}_{\Lambda,\hat{s}}\frac{\sigma}{2}f^{s}_{\Lambda,\hat{s}} \tag{37}$$

where $(\Lambda,\hat{s})$ are as defined earlier and $\Lambda^*_{\hat{s}}$ is the window width along $\hat{s}$ at the fixed point. $f^{c;\dagger}_{\Lambda,\hat{s}} = \left[c^{\dagger}_{\Lambda,\hat{s},\sigma}\,c_{-\Lambda,T\hat{s},-\sigma}\right], f^{s;\dagger}_{\Lambda,\hat{s}} = \left[c^{\dagger}_{\Lambda,\hat{s},\sigma}\,c^{\dagger}_{\Lambda-2\Lambda^*_{\hat{s}},T\hat{s},-\sigma}\right]$, are the spinorial representation for a pair of Fermions. This Hamiltonian is easily seen as a sum of mutually commuting Hamiltonian of one-dimensional systems, each involving a distinct pair of normal directions $(\hat{s}, T\hat{s})$. H^* represents the Hamiltonian for the gapless parts. This results from the fact that tangential scattering between different $\hat{s}$ directions is RG irrelevant. Further, as each of these 1D Hamiltonians involves scattering across all ranges in momentum-space, the scattering vertices $K^*_{c,\hat{s}}(\omega))$ and $K^*_{s,\hat{s}}(\omega))$ are inversely proportional to the number of states along a given $\hat{s}$: $K^*_{c,\hat{s}}(\omega)) \sim U_0/\sqrt{\mathrm{Vol}}$, $K^*_{s,\hat{s}}(\omega)) \sim U_0/\sqrt{\mathrm{Vol}}$ where Vol is the no. of lattice sites.

The charge/spin pseudospin flip scattering terms $(A^+_{*,\hat{s}}A^-_{*,-\hat{s}} + \mathrm{h.c.})/(S^+_{*,\hat{s}}S^-_{*,-\hat{s}} + \mathrm{h.c.})$ present in the fixed point Hamiltonian equation (36) comprise the charge/spin backscattering processes for resonant pairs ($\delta = 0$). We had earlier shown in equation (19) the appearance of log-divergences in the 2nd order

corrections of the T-matrix arising from scattering in the resonant-pair subspaces. Here, through the RG flow, we show the condensation of the pseudospins in these subspaces

$$\hat{n}_{\mathbf{k}_{\Lambda_j\hat{s}}\sigma} = \hat{n}_{\mathbf{k}_{-\Lambda_j T\hat{s}}-\sigma} \to (\mathbf{A}_{\Lambda\hat{s}})^2 = \frac{3}{4}\,,\ \hat{n}_{\mathbf{k}_{\Lambda_j\hat{s}}\sigma} = 1 - \hat{n}_{\mathbf{k}_{\Lambda_{j-2\Lambda^*_{\hat{s},\omega}}T\hat{s}}-\sigma} \to (\mathbf{S}_{\Lambda\hat{s}})^2 = \frac{3}{4}. \tag{38}$$

The fixed point values of the backscattering couplings are given by

$$\left[\omega - p\frac{\epsilon^*_l + \epsilon^*_{l'}}{2} - (1-p)\frac{\epsilon^*_l - \epsilon^*_{l'}}{2}\right] = \frac{K^*_{p,\hat{s}}}{4}. \tag{39}$$

The topological indices $N^{\Uparrow}_{\hat{s}}(\omega)$ and $N^{\Downarrow}_{\hat{s}}(\omega)$ appearing in equation (36) characterise the pseudogap phase as follows

$$\begin{aligned} \mathrm{I}: N^{\Uparrow}_{\hat{s}}(\omega) = 1 - N^{\Downarrow}_{\hat{s}}(\omega) = 1 \quad \forall\,\hat{s} \in [\hat{s}_{AN}, \hat{s}']\,, \\ \mathrm{II}: N^{\Downarrow}_{\hat{s}}(\omega) = 1 - N^{\Uparrow}_{\hat{s}}(\omega) = 1 \quad \hat{s} \in [\hat{s}', \hat{s}_{\mathrm{N}}]. \end{aligned} \tag{40}$$

In this way, the first term in Hamiltonian $H^*(\omega)$ describes the gapped parts of the FS (I in equation (40)), while the second term $H^{3*}(\omega, \hat{s})$ (of the form equation (31)) describes the gapless terms of the FS (II in equation (40)) in terms of composites of 2e–1h degrees of freedom. At the second Lifshitz transition involving the gapping of the FS at the nodes, $\hat{s}' = \hat{s}_{\mathrm{N}}$ and the resulting Mott liquid (discussed in more detail in section 6) is described by the global topological invariant $N^{\Uparrow}_{\hat{s}}(\omega) = 1 \quad \forall\hat{s}$. The pseudogap phase is thus a coexistence of gapped and gapless parts of the FS, and can also be characterised by a different global topological invariant

$$N^{\mathrm{PG}}_{\hat{s}} = N_{R\hat{s}} + N_{T\hat{s}}\,, \tag{41}$$

where $N_{R/T\hat{s}} = |N^{\Uparrow}_{\hat{s}}(\omega) - N^{\Uparrow}_{\hat{s}+(R/T)\hat{s}}(\omega)|$, and the parity operation $R\hat{s}: \hat{s}_x \leftrightarrow \hat{s}_x, :\hat{s}_y \leftrightarrow -\hat{s}_y$ (or vice versa). It is easily seen that $N^{\mathrm{PG}}_{\hat{s}} = 1 \quad \forall\,\hat{s}$ in the PG phase, and vanishes in the metallic and insulating phases. These non-local order parameters ensure that the two $T = 0$ Fermi surface topology-changing Lifshitz transitions at the passage into and out of the pseudogap phase do not belong to the Ginzburg–Landau–Wilson paradigm [66].

6. Properties of the Mott liquid

In the energy range $\frac{W}{2} > \omega > \omega_{\mathrm{ins}}$, the spin-charge interplay parameter is found to be $p = 0$ (equation (23)). In turn, this makes the RG flow for the Umklapp process marginal, such that we obtain the fixed point coupling $K^*_{\mathrm{c}}(\omega) = \bar{U}_0$. Then, using the RG invariant relation equation (24), we obtain the fixed point value for the spin backscattering coupling as

$$K^*_{\mathrm{s}}(\omega) = \frac{\bar{U}_0(1-p)K^*_{\mathrm{c}}(\omega)}{K^*_{\mathrm{c}}(\omega) - p\bar{U}_0}|_{p=0,K^*_{\mathrm{c}}(\omega)} = \bar{U}_0. \tag{42}$$

Thus, we obtain the fixed point Hamiltonian for the Mott liquid state as

$$\hat{H}^*(\omega) = \sum_{\hat{s}} \bar{U}_0 \left[\mathbf{A}_{*,\hat{s}} \cdot \mathbf{A}_{*,-\hat{s}} - \mathbf{S}_{*,\hat{s}} \cdot \mathbf{S}_{*,-\hat{s}}\right]\,, \tag{43}$$

where the psuedospins $\mathbf{A}_{*,\hat{s}}$ and $\mathbf{S}_{*,\hat{s}}$ are as defined in earlier sections. As mentioned in an earlier section, this Hamiltonian is again a collection of 1D Hamiltonians, and the renormalised coupling $\bar{U}_0$ is therefore given by $\bar{U}_0 = U_0/\sqrt{\mathrm{Vol}}$. The Hamiltonian thus obtained has antiferromagnetic and ferromagnetic exchange interactions in the charge-type pseudospin and spin-type pseudospin sectors respectively. A temperature scale T_{ML} associated with the formation of the gapped Mott liquid can be obtained by using the connection between a quantum fluctuation scale and a thermal scale (equation (18)) as follows. From the form of the two electron Hartree self energy contribution $K^*_{p,\hat{s}}$ and equation (18),we determine T_{ML} as

$$T_{\mathrm{ML}} = \frac{\hbar}{k_{\mathrm{B}}}\max_{\hat{s}}\tilde{\omega}_{\hat{s}} = \frac{\hbar N^*(\hat{s}_1, 0)}{2k_{\mathrm{B}}}\left(\epsilon_{\Lambda_0,\hat{s}_{\mathrm{N}}} - \epsilon_{\Lambda^{**}(\omega_{ins}),\hat{s}_{\mathrm{N}}}\right), \tag{44}$$

where the normal $\hat{s}_1 = \left(1 - \frac{\Lambda_0}{\sqrt{2}\pi}\right)\hat{s}_{\mathrm{AN}}$ is defined in the immediate vicinity of $\hat{s}_{\mathrm{AN}}$ in order to avoid the discontinuity at the van Hove points. The normal distance $\Lambda^{**}(\omega_{\mathrm{ins}})$ is obtained from the equation (30).

6.1. Low energy eigenstates of the Mott liquid

Some of the many-body eigenstates for H (equation (43)) are obtained by entangling every charge pseudospin with a unique pair of occupied electronic states residing outside the window, such that the spin pseudospins have vanishing magnitude ($(\mathbf{S}_{\Lambda\hat{s}})^2 = 0$). We now lay out the construction of such states. The vacuum state along a pair of normal $\hat{s}$ is given by

$$|0\rangle_d = |[0_{1'}0_1 0_{-1}0_{-1'}]\cdots[0_{1'}0_1 0_{-1}0_{-1'}]\cdots[0_{n'}0_n 0_{-n}0_{-n'}]\rangle_d\,, \tag{45}$$

where the labels $(j,d) := \mathbf{k}_{\Lambda_j\hat{s}},\sigma$ and $(-j,d) := \mathbf{k}_{-\Lambda_j,T\hat{s}},-\sigma$ represent momentum vectors *within* the emergent window $\Lambda_j < \Lambda^*_{\hat{s}}$. On the other hand, the labels $(j',d) := \mathbf{k}_{\Lambda_{j-2\Lambda^*_{\hat{s}}},\hat{s}},\sigma$, $(-j',d) = \mathbf{k}_{\Lambda_{j-2\Lambda^*_{\hat{s}}},\hat{s}},-\sigma$ represent the momentum vectors residing *outside* the emergent window $\Lambda^*_{\hat{s}} < |\Lambda_j - 2\Lambda^*_{\hat{s}}|$. The boundary states of the emergent window are represented by $(n,d) = \mathbf{k}_{\Lambda_{j^*}\hat{s}},\sigma$ and $(-n,d) = \mathbf{k}_{-\Lambda_{j^*}T\hat{s}},-\sigma$.

We denote the configurations of a single charge pseudospin and its associated pair of electronic states by

$$|\uparrow_j\rangle_d := |1_{\mathbf{k}_{\Lambda_j\hat{s}}\sigma}1_{\mathbf{k}_{-\Lambda_j,T\hat{s}},-\sigma}\rangle,\ |\downarrow_j\rangle_d := |0_{\mathbf{k}_{\Lambda_j\hat{s}},\sigma}0_{\mathbf{k}_{-\Lambda_j,T\hat{s}},-\sigma}\rangle. \tag{46}$$

The vacuum can then be rewritten in the charge pseudospin basis

$$|0\rangle_d = |[0_{1'}\downarrow_1 0_{-1'}]\cdots[0_{2'}\downarrow_2 0_{-1'}]\cdots[0_{n'}\downarrow_n 0_{-n'}]\rangle_d = |A_{*,\hat{s}} = N^*_{\hat{s}}, A^z_{*,\hat{s}} = -N^*_{\hat{s}}\,,\rangle \tag{47}$$

where $2N^*_{\hat{s}}$ is the number of charge pseudospins along $\hat{s}$. The application of operator $M^+_{k,d} = c^\dagger_{j,d}A^+_{j',d}c^\dagger_{-j',d}$ flips a charge pseudospin in the $\uparrow$ configuration along with creating electrons in two associated states: $M^+_{j,d}|0\rangle = |[1_{j'}\uparrow_j 1_{-j'}]\rangle_d$. From the above operation, it can be easily seen that for every charge pseudospin-flip operation, a pair of electrons created outside the window get entangled. Further, we find that the spin pseudospin raising and lowering operators annihilate this composite space

$$S^\pm|[1_{j'}\uparrow_j 1_{-j'}]\rangle = 0\,,\ S^\pm|[0_{j'}\downarrow_j 0_{-j'}]\rangle = 0\,. \tag{48}$$

The z-component can also be shown to vanish in a similar fashion. With these constraints, we can now determine eigenstates of the total charge pseudospin angular momentum operator along $\hat{s}$ $\mathbf{A}_{*,\hat{s}} = \sum_{\Lambda=0}^{\Lambda^*_{\hat{s}}}\mathbf{A}_{\Lambda\hat{s}}$

$$|A_{*,\hat{s}} = N = A^z_{*,\hat{s}}\rangle = \sum_{j_1,\cdots,j_l}\begin{vmatrix} e^{ij_1q_1} & \cdots & e^{ij_1q_l}\\ \vdots & \ddots & \vdots\\ e^{ij_lq_1} & \cdots & e^{ij_lq_l}\end{vmatrix}\prod_i M^+_{j_i,d}|0\rangle_d \tag{49}$$

where the Slater determinant involves states with wavevectors $q_s = \frac{s\pi}{2N^*_{\hat{s}}} \in [-\pi,\pi)$, $l = N + N^*_{\hat{s}}$. The eigenvalue of $\mathbf{A}^2_{*,\hat{s}}$ for the state $|A_{*,\hat{s}} = N = A^z_{*,\hat{s}}\rangle$ is given by $A^2_{*,\hat{s}} = N(N+1)$. This can be obtained by noting that

$$\mathbf{A}^2_{*,\hat{s}} = \frac{3}{4}(2N^*_{\hat{s}}) + \sum_{i<j=1}^{2N^*_{\hat{s}}}P_{ij} - \frac{1}{2}\begin{pmatrix}2N^*_{\hat{s}}\\ 2\end{pmatrix} \tag{50}$$

where $P_{ij} = \left(2\mathbf{A}_{\Lambda_i\hat{s}}\cdot\mathbf{A}_{\Lambda_j\hat{s}} + \frac{1}{2}\right)$ is the permutation operator that exchanges the i and j charge pseudospin configurations.

One class of eigenstates for the Hamiltonian in equation (43) can now be obtained by entangling states $|A_{*,\hat{s}} = N, A^z_{*,\hat{s}} = p\rangle$ from one side of Fermi surface with $|A_{*,-\hat{s}} = N, A^z_{*,-\hat{s}} = p\rangle$ from the diametrically opposite side

$$\begin{aligned}|A_* = m, A^z_* = p, A_{*,\hat{s}} = N_1, A_{*,-\hat{s}} = N_2\rangle \\ = \sum C^{m,p}_{N_1,p_1;N_2,p_2}\times|A_{*,\hat{s}} = N_1, A^z_{*,\hat{s}} = p_1; A_{*,-\hat{s}} = N_2, A^z_{*,-\hat{s}} = p_2\rangle\end{aligned} \tag{51}$$

where $p_1 = p - p_2$ and $C^{m,p}_{N_1,p_1;N_2,p_2}$ are Clebsch–Gordon coefficients [74]. The energy eigenvalues for these states are then obtained as

$$E = \sum_{\hat{s}}\frac{\bar{U}_0}{2}[m(m+1) - N_1(N_1+1) - N_2(N_2+1)]. \tag{52}$$

From the expression, we observe that low-lying eigenstates of the spectrum reside in the space of states

$$|\Psi_{\hat{s}}, m\rangle = |A_* = m, A_{*,\hat{s}} = A_{*,-\hat{s}} = N^*_{\hat{s}}, S_{\Lambda\hat{s}} = 0\rangle\,, \tag{53}$$

where the charge pseudospin angular momentum of the two normal directions $\hat{s}$ and $-\hat{s}$ have magnitude $N^*_{\hat{s}}(N^*_{\hat{s}}+1)$. The eigenvalue of the Hamiltonian $H^*(\omega)|\Psi_{\hat{s},m}\rangle = E^c_m|\Psi_{\hat{s},m}\rangle$ associated with the eigenstates equation (53) are

$$E^c_m = \sum_{\hat{s}} \bar{U}_0 \frac{1}{2}\left(m(m+1) - 2N^*_{\hat{s}}\left(N^*_{\hat{s}}+1\right)\right), \tag{54}$$

where $N^*_{\hat{s}}$ is the number of states in the window $\left[0, \Lambda^*_{\hat{s}}\right]$ and $0 \leqslant m \leqslant 2N^*_{\hat{s}}$. The lowest lying eigenstate $|\Psi_{\hat{s}}, 0\rangle$ is obtained for $m = 0$, i.e., a charge pseudospin singlet with energy $E_1 = -\bar{U}_0 \sum_{\hat{s}} N^*_{\hat{s}}\left(N^*_{\hat{s}}+1\right)$.

Another family of eigenstates

$$|\Phi_{\hat{s}}, m\rangle = |S_* = m, S_{*,\hat{s}} = S_{*,-\hat{s}} = N^*_{\hat{s}}, A_{\Lambda\hat{s}} = 0\rangle \tag{55}$$

is obtained from the spin pseudospin subspace $\mathbf{S}^2_{\Lambda\hat{s}} = \frac{3}{4}$, and where all the individual charge pseudospins $\mathbf{A}_{\Lambda\hat{s}} = 0$. The energy spectrum for this class of wave functions, $H^*(\omega)|\Phi_{\hat{s},m}\rangle = E^s_m|\Phi_{\hat{s},m}\rangle$, is given by

$$E^s_m = -\sum_{\hat{s}} \bar{U}_0 \frac{1}{2}\left(m(m+1) - 2N^*_{\hat{s}}\left(N^*_{\hat{s}}+1\right)\right), \tag{56}$$

where $m \in (0, 2N^*_{\hat{s}})$ once again. For the lowest lying eigenstate $m = 2N^*_{\hat{s}}$ configuration, the energy is given by $E_2 = -\bar{U}_0 \sum_{\hat{s}} N^{*2}_{\hat{s}}$.

But have we accounted for all the states within the window $\Lambda^*_{\hat{s}}$? An answer can be found by first computing the size of the Hilbert space for the Hamiltonian $H^*(\omega)$. By choosing every pair of two states $(\Lambda, \hat{s}), (-\Lambda, T\hat{s})$, where $\Lambda < \Lambda^*_{\hat{s}}$, there are two more electronic states that are chosen accordingly, i.e., $(\Lambda - 2\Lambda^*_{\hat{s}}, \hat{s}), (-\Lambda - 2\Lambda^*_{T\hat{s}}, T\hat{s})$. Thus, the total size of the Hilbert space within the window $\Lambda^*_{\hat{s}}$ is given by $2^{2N^*_{\hat{s}}}$. On the other hand, the total number of eigenstates of type $|\Psi_{\hat{s}}, m\rangle$ is $2^{N^*_{\hat{s}}}$, as there are 2 choices per composite subspace (equation (46)) and there are $N^*_{\hat{s}}$ such subspaces. An identical count of $2^{N^*_{\hat{s}}}$ is obtained similarly for the Hilbert space of the states $|\Phi_{\hat{s}}, m\rangle$. Therefore, these two sets of eigenstates do not exhaust the entire eigenspectrum; there are other exotic combinations of entangled states possible, whose count is $2^{2N^*_{\hat{s}}} - 2^{N^*_{\hat{s}}+1}$.

The state spaces equations (53) and (55) have been chosen such that they possess either $\langle(\Delta S^{x,y,z}_{\Lambda\hat{s}})^2\rangle = 0$ or $\langle(\Delta A^{x,y,z}_{\Lambda\hat{s}})^2\rangle = 0$. This sets them out as excellent candidate members of the low energy spectrum: any locally spin-charge combination must, on the other hand, involve non-zero uncertainties $\langle(\Delta S^{x,y,z}_{\Lambda\hat{s}})^2\rangle \neq 0$ as well as $\langle(\Delta A^{x,y,z}_{\Lambda\hat{s}})^2\rangle \neq 0$, raising their energy. We can now conclude on the ground states of $H^*(\omega)$. Clearly, $|\Psi_{\hat{s}}, m = 0\rangle$ and $|\Phi_{\hat{s}}, m = 2N^*_{\hat{s}}\rangle$ are the lowest energy states (with energies E_1 and E_2 respectively. In order for them to be degenerate ground states, we need to take the thermodynamic limit $N^*_{\hat{s}} >> 1$, such that $N^{*2}_{\hat{s}} > N^*_{\hat{s}}$ leading to $E_1 = E_2 \equiv E_g$. Further, in this limit, the sum and difference combinations of the states equations (53) and (55)

$$|\Gamma_\pm, m\rangle = \prod_{\hat{s}} \frac{1}{\sqrt{2}}\left[|\Psi_{\hat{s}}, m\rangle \pm |\Phi_{\hat{s}}, 2N^*_{\hat{s}} - m\rangle\right] \tag{57}$$

are also eigenstates of $H^*(\omega)$.

One of the lowest excitations lying above these ground states can be written by noting that the magnitude of the pseudospins $A^{\hat{s}}_*$ and $A^{-\hat{s}}_*$ are lowered from $N^*_{\hat{s}}$ to $N^*_{\hat{s}} - 1$, such that the charge pseudospin singlet formed from these two has the form

$$|A_* = 0, A_{*,\hat{s}} \equiv A_{*,-\hat{s}} = N^*_{\hat{s}} - 1, S_{\Lambda\hat{s}} = 0\rangle. \tag{58}$$

Similarly, another lowest lying excitation is given by

$$|A_{\Lambda\hat{s}} = 0, S_* = 2N^*_{\hat{s}} - 2, S_{*,\hat{s}} \equiv S_{*,-\hat{s}} = 2N^*_{\hat{s}} - 2\rangle. \tag{59}$$

The energy cost to reach the lowest lying excited state (i.e., the spectral gap) in the thermodynamic limit ($N^*_{\hat{s}} >> 1$) is also easily obtained as $\Delta E = \bar{U}_0 \sum_{\hat{s}} N^*_{\hat{s}}$.

6.2. Topological features of the Mott liquid

By putting periodic boundary conditions on the momentum-space window, we can construct a set of nonlocal operators W_m

$$W_m = \exp\left[\mathrm{i}\frac{\pi}{2}(|\Gamma_+, m\rangle\langle\Gamma_+, m| - |\Gamma_-, m\rangle\langle\Gamma_-, m| - 1)\right],$$

such that W_m commutes with the $SU(2) \times SU(2)$ pseudospin rotational invariant Hamiltonian in the projected subspace of $P_c + P_s$

$$[(P_c + P_s)H^*(P_c + P_s), W_m] = 0 \,\forall\, m, \tag{60}$$

where the projection operators are given by $P_c = \sum_m |\Psi_{\hat{s}}, m\rangle\langle\Psi_{\hat{s}}, m|$ and $P_s = \sum_m |\Phi_{\hat{s}}, m\rangle\langle\Phi_{\hat{s}}, m|$. Further, it is clear that $W_m|\Gamma_\pm, m\rangle = \pm|\Gamma_\pm, m\rangle$. Thus, the simultaneous degenerate ground state eigenfunctions of the Hamiltonian H^* of the Mott liquid and the operator $W_{m=0}$ can be written as

$$|\Gamma_\pm, 0\rangle = \prod_{\hat{s}} \left[\frac{1}{\sqrt{2}}\left(|\Psi_{\hat{s}}, 0\rangle \pm |\Phi_{\hat{s}}, 2N^*_{\hat{s}}\rangle\right)\right]. \tag{61}$$

These two degenerate ground states are connected via a twist operator/ nonlocal gauge transformation $\hat{O}$

$$\hat{O} = \exp\left[4\pi \mathrm{i} \sum_{\Lambda\hat{s}} \frac{(S^z_{\Lambda\hat{s}})^2}{N^*_{\hat{s}}}\right], \; \hat{O}|\Gamma_\pm, 0\rangle = |\Gamma_\mp, 0\rangle. \tag{62}$$

As these two states are protected by the many body gap $\Delta E = \bar{U}_0 \sum_{\hat{s}} N^*_{\hat{s}}$ (where $\bar{U}_0 = U_0/\mathrm{vol}$) given above, adiabatic passage between these degenerate ground states via the application of the twist operator $\hat{O}$ involve the creation of charge-1/2 excitations [75–77], seen from the anticommutation relation $\{\hat{O}, W_0\} = 0$. The above relation, along with $[\hat{O}^2, W_0] = 0$, allows us to conclude that the ground state manifold is *topologically* degenerate in the thermodynamic limit.

6.3. Benchmarking against existing numerical results

In order to benchmark the results obtained from the effective low-energy Hamiltonian and wavefunctions given above against those found from existing numerical methods applied to the 2D Hubbard model on the square lattice [11, 44, 45], we present results for the ground state energy per particle E_g and the fraction of bound pairs (Bp) in the gapped Mott liquid ground state. The analytic forms of E_g and Bp are computed from the spin and charge backscattering parts of the effective Hamiltonian given above ($H^*(\omega)$) and are found to be

$$E_g = \frac{E_2}{N_e} = -\sum_{\hat{s}} \frac{\bar{U}_0 (N^*_{\hat{s}})^2}{N_e}, \; \mathrm{Bp} = \frac{\sum_{\hat{s}} N^*_{\hat{s}}}{N_e}, \; \mathrm{Ubp} = 1 - \mathrm{Bp}, \tag{63}$$

where the fraction of unbound pairs is denoted by Ubp. The plots for E_g and (Bp, Ubp) versus the probe energy scale ω are shown in figures 9(a) and (b) respectively. A comparison of the saturation value of the ground state energy for the largest k-space grid used in our simulations ($2^{15} \times 2^{15}$), $E^*_g = -0.526\, t$ (shown in figure 9), is well within the range $-0.51t < E_{gs} < -0.53\, t$ obtained in the thermodynamic limit from several state-of-the-art numerical methods applied to the half-filled 2D Hubbard model at $U = 8\, t$ [11, 44, 45]. Similarly, the average saturation value for the fraction of unbound pairs (Ubp*) in the Mott liquid obtained from a finite-size scaling analysis (inset of figure 9), Ubp$^* \sim 0.051$, lies slightly below the range $0.0535 < \mathrm{Ubp} < 0.0545$ obtained in reference [11]. The code used for the numerical computation of the ground state energy shown here is made available electronically [47].As an added note, we point the reader to further benchmarking exercises presented in C for the cases of $U/t = 2, 4, 6, 10$ at half-filling. We continue to find excellent quantitative agreement with exact diagonalization studies from reference [45] and other numerical methods reported in references [11, 44]. We stress that this offers confidence in the effective Hamiltonian and ground-state wavefunction we have obtained for the half-filled Mott liquid.

6.4. Symmetry breaking of the Mott liquid: Néel antiferromagnetism

Our RG analysis can also be extended to show that the topologically ordered Mott liquid ground state is replaced, under renormalisation, by a chosen ordered state with an order parameter corresponding to a defined broken symmetry. As RG transformations are, by definition, meant to preserve the symmetries of the Hamiltonian they act upon, such symmetry-broken states can only be reached from our RG analysis by first explicitly including an order parameter-field term in the Hamiltonian and then proceeding with the RG transformations [78]. In this way, we can reach a (π, π) spin density wave (SDW) Neél ground state in the presence of a staggered magnetic field (h). Using the Hamiltonian renormalization equation given earlier, we find the RG equation for the tangential Umklapp scattering processes: scattering between the neighbourhood of different antinodal patches, is given in terms of the dimensionless coupling $V'_\Lambda = \frac{V_\Lambda}{h_\Lambda}$ as

$$\Delta V'_{\Lambda_j} = \frac{\Delta V'_{\Lambda j}}{\Delta \log \frac{\Lambda_j}{\Lambda_0}} = N_\Lambda \frac{V'^2_{\Lambda_j}}{1 - V'_{\Lambda_j} N_\Lambda (N_\Lambda + 1)}. \tag{64}$$

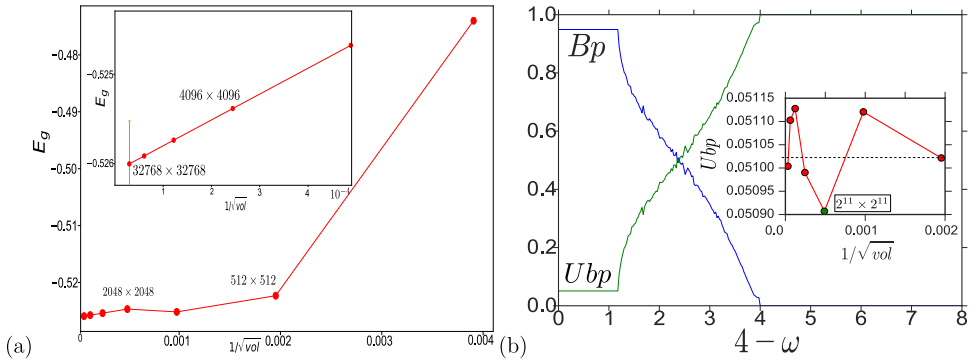

Figure 9. (a) Finite-size scaling of the saturation value for $E_g \equiv E_{gs}$ with $1/\sqrt{\text{Vol}}$ with increasing k-space grid size from $2^8 \times 2^8$ to $2^{15} \times 2^{15}$. The saturation E_{gs} for the largest grid is observed to be -0.526 (for $t = 1$). The error bar for all data points is $\sim O(10^{-4}t)$. Inset: zoomed view of finite-size scaling plot for lattice sizes $2^{11} \times 2^{11}$ to $2^{15} \times 2^{15}$. (b) Blue curve: growth/decay in fraction of bound/unbound pairs (Bp, Ubp) across the phase diagram with varying ω. Inset: finite-size scaling of the saturation value for the fraction of unbound pairs (Ubp*) in the Mott liquid with $1/\sqrt{\text{vol}}$. The saturation fraction display small fluctuations about an average value Ubp$^* \sim 0.051$. Error bar for all data points is $\sim O(10^{-5})$.

Note that $\Lambda_j = \Lambda_0 \exp(-j)$ and $\Lambda_{j-1} = \Lambda_0 \exp(-(j-1))$, such that $\Delta \log \frac{\Lambda_j}{\Lambda_0} = 1$. Here, N_Λ is the number of states near the AN $((0, k_y), (k_x, 0))$ region at distance Λ from it. Given the flat geometry of the quadratic dispersion $\epsilon_{k_y,0} = k_y^2/2$ near the AN the density of states diverges logarithmically $N_\Lambda = \ln|\Lambda_0/\Lambda|$. For weak coupling $V'_\Lambda \ll 1/N_\Lambda(N_\Lambda + 1)$, we find the continuum form of the RG equation as,

$$\frac{\mathrm{d}V'_\Lambda}{\mathrm{d}\,\ln\frac{\Lambda}{\Lambda_0}} = \ln|\frac{\Lambda_0}{\Lambda}|V'^2_\Lambda \rightarrow V_\Lambda = \frac{U_0}{1 + \left(\log\frac{\Lambda}{\Lambda 0}\right)^2 \frac{U_0}{2h}} \rightarrow \frac{\Lambda}{\Lambda_0} = \exp\left(-\frac{2h}{\sqrt{U_0}}\right), \tag{65}$$

where the RHS of the equation possesses the logarithmic divergence [79–81]. In this way, we find the well-known form for the gap function Λ corresponding to the Néel SDW state obtained from a mean-field analysis [82].

6.5. Cooper-pair fluctutations within the Mott liquid

The pseudospin flip interaction $-\bar{U}_0(S^+_{*,\hat{s}}S^-_{*,-\hat{s}} + \text{h.c.})$ present within the Mott liquid can be rewritten in terms of interactions between finite-momentum Cooper pairing terms as follows:

$$\sum_{\Lambda\Lambda'}\left[S^+_{\Lambda\hat{s}}S^-_{\Lambda'\hat{s}} + \text{h.c.}\right] = \sum_{\mathbf{k},\mathbf{p}} c^\dagger_{\mathbf{k}\uparrow}c^\dagger_{\mathbf{p}-\mathbf{k}\downarrow}c_{\mathbf{p}-\mathbf{k}'\downarrow}c_{\mathbf{k}'\uparrow}, \tag{66}$$

where $\mathbf{k} = \mathbf{k}_{\Lambda,\hat{s}}$ and $\mathbf{k}' = \mathbf{k}_{2\Lambda^*_{\hat{s}}-\Lambda,\hat{s}}$. This obervation will be shown to coincide with the presence of a decayingoff-diagonal long range order (ODLRO). The presence of entanglement between the charge/spin type pseudospins in equation (61), along with mixing between different $\mathbf{p}$-momentum pairs, is captured in the off-diagonal long range order ODLRO,

$$\rho(\mathbf{r}-\mathbf{r}') = \langle\Psi_1|\psi^\dagger_{\mathbf{r}\uparrow}\psi^\dagger_{\mathbf{r}\downarrow}\psi_{\mathbf{r}'\downarrow}\psi^\dagger_{\mathbf{r}'\uparrow}|\Psi_1\rangle = \frac{1}{2}\sum_{\hat{s},\mathbf{p}=0}^{2\Lambda^*_{\hat{s}}}\frac{N_{\Lambda^*_{\hat{s}}}}{L^2}\cos(\mathbf{p}\cdot(\mathbf{r}-\mathbf{r}')). \tag{67}$$

Here, we have chosen the quantization axis of $\mathbf{S}_{\Lambda\hat{s}}$ along the x-direction. From this expression, we observe that the ODLRO decays for $|(\mathbf{r}-\mathbf{r}')\cdot\hat{s}| > (2\Lambda^*_{\hat{s}})^{-1}$. The prefactor of $1/2$ in the expression for the ODLRO arises from the superposition of the two types of many body states (equation (61)), while its anisotropic form results from the geometry of the Fermi surface in the tight-binding problem. Finally, $N_{\Lambda^*_{\hat{s}}}$ is the number of composite objects along the $\hat{s}$ direction. We saw earlier the susceptibility of the Mott liquid towards a symmetry-broken Néel antiferromagnet. From the analysis presented for the ODLRO above, we find that the global spin-charge entanglement prevents the condensation of zero-momentum Cooper pairs. This leads us to conclude that antiferromagnetism is clearly favoured over a $U(1)$-symmetry broken superconducting state as an instability of the Mott liquid, consistent with the finding of subdominant superconducting correlations in the insulating phase at half-filling from VMC studies [83].

7. Conclusions and perspectives

There are several interesting consequences of our RG analysis of the 2D Hubbard model on the square lattice, and we now discuss each of these in turn. At the very outset, we wish to stress that the simplicity of the Hubbard Hamiltonian (i.e., possessing effectively only a single parameter U/t) offers the possibility that several of our results are of likely importance for the broad understanding of the phenomenology of bandwidth-driven Mott transitions in a variety of strongly correlated electronic systems with strong electronic differentiation arising from the tight binding dispersion [2]. Thus, even as our results are immediately relevant to the physics of correlated electrons on bipartite lattices with unfrustrated interactions and hoppings, we expect that they offer insight on systems in which these restrictions have been lifted.

First among our findings is the fact that in the RG phase diagram (figure 4), the low-energy ground state is Mott insulating for any Hubbard repulsion $U > 0$ at $1/2$-filling. The absence of a critical Hubbard coupling U^* at $1/2$-filling is consistent with the results of several recent numerical investigations of the problem (references [20–22, 22–25]). Further, our study pinpoints the marginal Fermi liquid as the parent metal of the insulating Mott liquid state. All of this provides evidence for the fact that the Mott metal–insulator transition of the 2D Hubbard model is truly nonperturbative in nature, and inaccessible via a weak-coupling many-body perturbation theory about the Fermi liquid fixed point (adiabatically continuous to the non-interacting electron gas). Instead, our work reveals the nature of the FS topology-changing Mott metal-insulator transition at $T = 0$, highlighting the existence of a pseudogap phase as the pathway from the metallic to the insulating phase. This appears to confirm the conjecture of reference [67] on the nature of the $T = 0$ Mott transition.

The marginal Fermi liquid is found to arise from singular forward scattering in directions normal to the nested Fermi surface of the underlying tight-binding problem, causing the destruction of Landau quasiparticles and leading to a linear variation of resistivity with temperature. We derive analytically an effective Hamiltonian for the marginal Fermi liquid from the RG analysis. Importantly, this meets an oustanding formal challenge by providing a microscopic basis for the rich phenomenology of the marginal Fermi liquid theory. Remarkably, a computation of the quasiparticle residue of the 2e–1h constituents comprising the marginal Fermi liquid reveals that they are effectively non-interacting in the neighbourhood of the Fermi surface. This establishes firmly the marginal Fermi liquid theory as a paradigmatic fixed point theory for a non-Fermi liquid. In keeping with considerable recent activity in the area of holographic dualities, our results offer encouraging support in the search for other novel gapless states of quantum matter.

The pseudogap phase is observed to arise from the electronic differentiation encoded within the nested Fermi surface of the half-filled tight-binding model [67], and involves the gradual gapping of the Fermi surface (from antinodes to nodes [84]) via charge and spin excitations that are mutually entangled. We have clarified the topological quantum numbers (non-local order parameters) that quantify the passage through the pseudogap, as well as qualify as it as a phase of quantum matter distinct from the normal and Mott insulating phases. Our finding of pseudogap and non-Fermi liquid phases at $1/2$-filling also offer a natural explanation of experimental observations in the cuprates of such phases being proximate to the Mott insulating phase upon doping lightly with holes (see, e.g., [85]).

By obtaining analytically the many-particle wavefunctions for the Mott liquid phase at low energies, we demonstrate that it possesses signatures of topological order: a two-fold degeneracy of the ground state on the torus, and fractionally-charged topological excitations that interpolate between them. The ground state energy and double-occupancy fraction obtained from these wavefunctions, together with the effective Hamiltonian for the Mott liquid, display remarkable agreement with those obtained from state-of-the art numerical methods [11, 44, 45] for a wide range of the parameter $2 \leqslant U/t \leqslant 12$. Such microscopic insight into a topologically ordered gapped state of strongly correlated quantum matter has, to the best of our knowledge, seldom been available and constitutes a fundamental advance afforded by the RG method developed in this work. The benchmarking against results from numerical methods reinforces our confidence in the effective theory we have obtained for the Mott liquid phase, and paves the way for a systematic investigation of the many-particle entanglement of such an exotic state of quantum matter.

Importantly, upon including the possibility of symmetry-breaking within the RG formalism, the Mott liquid is found to turn into the familiar Néel spin-ordered charge-insulating Mott insulator. As we demonstrate in an accompanying work [86], this has important consequences for the nature of the hole-doped Mott insulator [46]. For instance, we will show there that the dominant charge gapping of the $1/2$-filled Mott liquid is steadily suppressed with hole-doping, leading to a novel quantum critical point. The subdominant Cooper pairing of the Mott liquid state at half-filling becomes dominant at this critical hole-doping, leading to a d-wave superconducting phase that surrounds the quantum critical point. Finally,

where do we expect some of our predictions to be tested experimentally? In recent years, cold fermionic gases have emerged as a leading contender for the study of strongly correlated fermionic systems (see, e.g., [87] for a recent review, and [88] for a recent experiment). Another possibility is the recent demonstration of the phenomenology of the high-temperature superconducting bulk cuprate systems in a monolayer crystal of $Bi_2Sr_2CaCu_2O_{8+\delta}$ [89]. Both systems offer exciting prospects in probing the 2D Mott–Hubbard transition in a controlled manner and at very low temperatures. Finally, as a particle–hole transformation on one of the sublattices of the 2D square lattices connects between the repulsive and attractive Hubbard models ([90]), we believe that our results are also significant in understanding the physics of the latter.

Acknowledgments

We dedicate this work to the memory of P W Anderson. The authors thank Sourav Pal, Apoorva Patel, H R Krishnamurthy, T V Ramakrishnan, S Mukherjee, T Das, A Garg, R K Singh, A Dasgupta, A Taraphder, S Sinha, M S Laad, G Baskaran, A M Srivastava, N S Vidhyadhiraja, S Kumar, B Bansal, S Raj, P Majumdar, S Pal, S Patra and M Patra for several discussions and feedback. AM thanks the CSIR, Govt. of India for funding through a junior and senior research fellowship. SL thanks the DST, Govt. of India for funding through a Ramanujan Fellowship during which a part of this work was carried out. We also thank two anonymous referees for their insightful comments and questions, as these helped improve the presentation immensely.

Appendix A. The Hamiltonian renormalization group flow

Starting from the Hamiltonian RG flow equation (15), and using the expressions for the unitary operator equation (10), we obtain

$$\Delta H_{(j)} = \sum_{l} \mathrm{Tr}_{j,l}(c^{\dagger}_{j,l} H_{(j)}) c_{j,l} G_{(j),l} c^{\dagger}_{j,l} \mathrm{Tr}_{j,l}(H_{(j)} c_{j,l}) \,, \tag{A.1}$$

where $G_{(j),l} = (\omega - \hat{n}_{j,l}\mathrm{Tr}_{j,l}(H^{D}_{(j)}\hat{n}_{j,l}))^{-1}$ and the diagonal Hamiltonian $H^{D}_{(j)}$ is given by

$$\begin{aligned}\mathrm{Tr}_{j,l}(H^{D}_{(j)}\hat{n}_{j,l}) = \epsilon_{j,l}\hat{n}_{j,l} + \sum_{l'} V^{(j)}_{l}(\delta)\left(\hat{n}_{j,l} - \frac{1}{2}\right)\left(\hat{n}_{j,l'} - \frac{1}{2}\right) \\ + \sum_{l''} L^{(j)}(\delta)\hat{n}_{j,l}\hat{n}_{j',l''} + \sum_{l''} R^{(j)}_{\delta\delta}\hat{n}_{j,l}\hat{n}_{j,l'}(1 - \hat{n}_{j,l''}) + \ldots \,.\end{aligned} \tag{A.2}$$

The various terms in $H^{D}_{(j)}$ are: the first term is the electronic dispersion ($\epsilon_{j,l}$), the term with coupling $V^{(j)}_{l}(\delta)$ is the longitudinal density–density interaction in the (ee–hh) and (eh–he) channels, the term with coupling $L^{(j)}(\delta)$ is the tangential density–density interaction and, finally, the term with coupling $R^{(j)}_{\delta\delta}$ is the 2e–1h interaction. The renormalization $\Delta H^{F}_{(j)}$ for the forward-scattering part of the Hamiltonian in the electron(e)–electron, hole(h)–hole, eh and he channels are obtained from equation (A.1) as

$$\begin{aligned}\Delta H^{F}_{(j)} = \sum_{k,k',l'} \Bigg[& c^{\dagger}_{k',l} c^{\dagger}_{k',l'} c_{j,l'} c_{j,l} \frac{(V^{(j)}_{l}(\delta))^2}{[G_{j,l}]^{-1} - V^{(j)}_{l}(\delta)\tau_{j,l}\tau_{j,l'}} c^{\dagger}_{j,l} c^{\dagger}_{j,l'} c_{k,l'} c_{k,l} \\ & + c^{\dagger}_{j,l} c^{\dagger}_{j,l'} c_{k',l'} c_{k',l} \frac{(V^{(j)}_{l}(\delta))^2}{[G_{j,l}]^{-1} - V^{(j)}_{l}(\delta)\tau_{j,l}\tau_{j,l'}} c^{\dagger}_{k,l} c^{\dagger}_{k,l'} c_{j,l'} c_{j,l} \\ & + c^{\dagger}_{k',l} c_{k,l'} c^{\dagger}_{j,l'} c_{j,l} \frac{(V^{(j)}_{l}(\delta))^2}{[G_{j,l}]^{-1} - V^{(j)}_{l}(\delta)\tau_{j,l}\tau_{j,l'}} c^{\dagger}_{j,l} c_{j,l'} c^{\dagger}_{k',l'} c_{k,l} \\ & + c^{\dagger}_{j,l} c_{j,l'} c^{\dagger}_{k',l} c_{k,l'} \frac{(V^{(j)}_{l}(\delta))^2}{[G_{j,l}]^{-1} - V^{(j)}_{l}(\delta)\tau_{j,l}\tau_{j,l'}} c^{\dagger}_{k',l'} c_{k,l} c^{\dagger}_{j,l'} c_{j,l} \Bigg] \\ = \sum_{k,k',l'} & c^{\dagger}_{k',l} c^{\dagger}_{k',l'} \frac{4(V^{(j)}_{l}(\delta))^2 \tau_{j,l}\tau_{j,l'}}{[G_{j,l}]^{-1} - V^{(j)}_{l}(\delta)\tau_{j,l}\tau_{j,l'}} c_{k,l'} c_{k,l} \,.\end{aligned} \tag{A.3}$$

Here, $(G_{j,l})^{-1} = \hat{\omega} - \epsilon_{j,l}\tau_{j,l} - \epsilon_{j,l'}\tau_{j,l'}$ is the inverse Green's function operator. The index (j, l) refers to the momentum and spin labelled state $|\mathbf{k}_{\Lambda_j,\hat{s}}, \sigma\rangle$, index (j, l') refers to the partner electronic state $|\mathbf{k}_{-\Lambda_j+\delta,T\hat{s}}, \sigma\rangle$. The index l essentially is a collective label that accounts for the normal direction $\hat{s}$ and spin σ. This labelling

scheme was defined just before equation (14) and here we are recalling it to bring clarity into the present discussion.

Finally, some remarks are in order on the similarities and differences with the weak coupling functional RG (FRG) for the 2D Hubbard model [91]. The states $|j,l\rangle$, $|j,l'\rangle$ located at a distance Λ_j from FS are disentangled at the RG step j, leading to renormalization of the forward scattering vertices. Similar to FRG, the states (j,l), (j,l') in the RG equations above are energetically proximate to the renormalized cutoff scale Λ, and are integrated out leading to the vertex flow equation. Additionally, note that in forward scattering RG equation (A.3), the first two lines comprise the nonperturbative renormalization in the ee/hh channel and account for the BCS diagrams. On the other hand, the last two lines comprise the renormalization in the eh/he channel and account for the ZS/ZS′ diagrams.

We can also observe the structural similarity of our RG equations to the one loop weak coupling RG equations obtained from FRG [27] by performing a Taylor expansion of the RG equation about small $V \ll 1$,

$$\Delta H^{F}_{(j)} = \sum_{k,k',l'} c^{\dagger}_{k',l} c^{\dagger}_{k',l'} c_{k,l'} c_{k,l} \left[\frac{4(V^{(j)}_{l}(\delta))^2 \tau_{j,l}\tau_{j,l'}}{\omega - \epsilon_{j,l}\tau_{j,l} - \epsilon_{j,l'}\tau_{j,l'}} - \frac{4(V^{(j)}_{l}(\delta))^3 \tau^2_{j,l}\tau^2_{j,l'}}{(\omega - \epsilon_{j,l}\tau_{j,l} - \epsilon_{j,l'}\tau_{j,l'})^2} + \cdots \right]. \tag{A.4}$$

The leading term in the RG equation (A.4) for $V^{(j)}_{l} << 1$ has denominator similar to that obtained from weak coupling FRG in the ee channel (BCS) [92]: $(\omega - \epsilon_{j,l}\tau_{j,l} - \epsilon_{j,l'}\tau_{j,l'})|1_{j,l}1_{j,l'}\rangle = 2^{-1}(\omega - \epsilon_{j,l} - \epsilon_{j,l'})$. Similarly, in the eh channel, the denominator of the RG equations have resemblance with terms ZS and ZS′ of weak coupling FRG [92]. The additional contribution of ω reflects the intrinsic quantum fluctuation energy scale (section 3.3), reflecting the retardation effects intrinsic to our RG procedure. As shown in equation (28), the RG of backscattering and three-particle vertices affect those of the 1 particle self energy Σ. The present discussion clarifies that the Σ obtained from our approach is consistent with that obtained from FRG.

Similarly, the renormalization $\Delta H^{\mathrm{B}}_{(j)}$ for backscattering terms is given by

$$\Delta H^{\mathrm{B}}_{(j)} = \sum_{k,k',l'} c^{\dagger}_{k',p} c^{\dagger}_{k',p'} \frac{4\, \mathrm{V}^{(j)}_{l}(\delta) K^{(j)}_{l}(\delta) \tau_{j,l}\tau_{j,l'}}{[G_{j,l}]^{-1} - V^{(j)}_{l}(\delta)\tau_{j,l}\tau_{j,l'}} c_{k,l'} c_{k,l}\,, \tag{A.5}$$

where the same Green's function operator has been used. The renormalization of the tangential scattering terms in the Hamiltonian can be similarly obtained by decoupling a collective configuration of states on the jth isogeometric curve

$$\Delta H^{\mathrm{T}}_{(j)} = \sum_{kk'} c^{\dagger}_{k,m} c^{\dagger}_{k,m'} \frac{(L^{(j)})^2 L^{+}_{j} L^{-}_{j}}{\hat{\omega} - \tilde{\epsilon}^{c}_{j,avg} L^{z}_{j} - L^{(j)} L^{z2}_{j}} c_{k',n'} c_{k',n}. \tag{A.6}$$

Here, $L^{+}_{j} = \sum_m c^{\dagger}_{j,m} c^{\dagger}_{j,m'}$, $L^{z}_{j} = 2^{-1}\sum_m (\hat{n}_{j,m} + \hat{n}_{j,m'} - 1)$ and L^{-}_{j} is the hermitian conjugate to L^{+}_{j}. The intermediate configurations of the states involved in the tangential scattering processes are labelled by

$$(j,m) = \mathbf{k}_{\Lambda_j \hat{s}}, \sigma), (j,m') = \mathbf{k}_{-\Lambda_j, T\hat{s}}, -\sigma),$$

$$(j,n) = \mathbf{k}_{\Lambda_j \hat{s}'}, \sigma), (j,n') = \mathbf{k}_{-\Lambda_j, T\hat{s}'}, -\sigma).$$

Using the angular momentum algebra $L^{+}_{j} L^{-}_{j} = L^{2}_{j} - L^{z2}_{j} - L^{z}$, we obtain

$$\Delta H^{\mathrm{T}}_{(j)} = \sum_{kk',m,n} c^{\dagger}_{k,m} c^{\dagger}_{k,m'} \frac{(L^{(j)})^2 (L^{2}_{j} - L^{z2}_{j} - L^{z}_{j})}{\hat{\omega} - \tilde{\epsilon}^{c}_{j,\mathrm{avg}} L^{z}_{j} - L^{(j)} L^{z2}_{j}} c_{k',n'} c_{k',n}. \tag{A.7}$$

The Hamiltonian RG for the 3-particle scattering vertices terms are obtained as

$$\begin{aligned}
\Delta H^{3}_{(j)} = & \sum_{k'',k',l',l''} c^{\dagger}_{k',l} c^{\dagger}_{k',l'} c_{j,l'} \frac{V^{(j)}_{l}(\delta) V^{(j)}_{l}(\delta')\tau_{j,l}}{\omega - \tilde{\epsilon}_{j,l}\tau_{j,l}} c^{\dagger}_{j,l''} c_{k'',l} c_{k'',l'} \\
& + \sum_{k'',p',l',l''} c^{\dagger}_{p',l} c^{\dagger}_{p',l'} c_{j,l'} \frac{K^{(j)}_{l}(\delta) K^{(j)}_{l}(\delta')\tau_{j,l}}{\omega - \tilde{\epsilon}_{j,l}\tau_{j,l}} c^{\dagger}_{j,l''} c_{k'',l} c_{k'',l'} \\
& + \sum_{\Lambda' < \Lambda_j, p', k''} c^{\dagger}_{p',l} c^{\dagger}_{p',l'} c_{j',l'} \frac{8 R^{(j)}_{l,\delta\delta''} R^{(j)}_{l,\delta'\delta''} \prod_{i=1}^{3} \tau_i}{[G_{j,l,3}]^{-1} - R^{(j)}_{l,\delta'',\delta''} \prod_{i=1}^{3} \tau_i} c^{\dagger}_{j',l''} c_{k'',l} c_{k'',l'}\,,
\end{aligned} \tag{A.8}$$

where the states are labelled by $i = 1 : (\mathbf{k}_{\Lambda_j \hat{s}}, \sigma)\,,\ 2 : (\mathbf{k}_{-\Lambda_j + \delta'', T\hat{s}}, -\sigma)\,,\ 3 : (\mathbf{k}_{\Lambda' \hat{s}}, \sigma)\,.$

Table C1. Ground state energy per site values obtained from the RG fixed points for $U/t = 2, 4, 6, 8, 10, 12$. The error bar for all data obtained from the RG is $O(10^{-4}t)$. Third column for $U/t = 2$, 4, 6, 8 and 12 represent the range of values obtained for the ground state per site for several different numerical methods [11, 44, 45].

U_0/t	E_g from RG at hole-fraction $f_h = 0$	Range of E_g from various numerical methods at $f_h = 0$ collated from [11, 45]
2	−1.199	(−1.176)–(−1.16)
4	−0.854	(−0.864)–(−0.85)
6	−0.652	(−0.658)–(−0.651)
8	−0.526	(−0.53)–(−0.51)
10	−0.439	−0.439
12	−0.367	(−0.369)–(−0.362)

Appendix B. The renormalized Hamiltonian at RG step *j*

The Hamiltonian at RG step j using flow equations equations (21), (26) and (27) is given by

$$
\begin{aligned}
H_{(j)}(\omega) = & \sum_{\Lambda<\Lambda_j} (\epsilon_{\Lambda\hat{s}} - \Delta\mu_{\text{eff}}) \left(\hat{n}_{\Lambda,\hat{s},\sigma} - \frac{1}{2}\right) + \sum_{\delta,\hat{s}\neq\pm\hat{s}'} L^{(j)(\omega)} c^{\dagger}_{\Lambda,\hat{s},\sigma} c^{\dagger}_{-\Lambda,T\hat{s},-\sigma} c_{-\Lambda',T\hat{s}',-\sigma} c_{\Lambda',\hat{s}',\sigma} \\
& + \sum_{\delta,\hat{s},\Lambda<\Lambda_j} (V^{(j)}_{c,l}(\omega) c^{\dagger}_{\Lambda,\hat{s},\sigma} c^{\dagger}_{-\Lambda+\delta,T\hat{s},-\sigma} c_{-\Lambda'+\delta,T\hat{s},-\sigma} c_{\Lambda',\hat{s},\sigma} + K^{(j)}_{c,l}(\omega) c^{\dagger}_{\Lambda,\hat{s},\sigma} c^{\dagger}_{-\Lambda+\delta,T\hat{s},-\sigma} c_{-\Lambda'-\delta,-T\hat{s},-\sigma} c_{\Lambda',-\hat{s},\sigma}) \\
& - \sum_{\delta,\hat{s},\Lambda<\Lambda_j} (V^{(j)}_{s,l}(\omega) c^{\dagger}_{\Lambda,\hat{s},\sigma} c_{-\Lambda+\delta,T\hat{s},-\sigma} c^{\dagger}_{\Lambda',T\hat{s},-\sigma} c_{2\Lambda+\Lambda'-\delta,\hat{s},\sigma} + K^{(j)}_{s,l}(\omega) c^{\dagger}_{\Lambda,\hat{s},\sigma} c_{-\Lambda+\delta,T\hat{s},-\sigma} c^{\dagger}_{\Lambda',-\hat{s},-\sigma} c_{\Lambda'+\delta-2\Lambda,-T\hat{s},\sigma}) \\
& + \sum_{\delta,\hat{s},\Lambda,\Lambda',\Lambda''<\Lambda_j} R^{(j)}_{l,\delta\delta'}(\omega) c^{\dagger}_{\Lambda,\hat{s},\sigma} c^{\dagger}_{-\Lambda+\delta,T\hat{s},-\sigma} c_{-\Lambda'+\delta,\hat{s},-\sigma} c^{\dagger}_{-\Lambda'+\delta',\hat{s},\sigma} c_{-\Lambda''+\delta',T\hat{s},-\sigma} c_{\Lambda'',\hat{s},\sigma} \,. \qquad \text{(B.1)}
\end{aligned}
$$

Appendix C. Benchmarking results for $2 \leqslant U/t \leqslant 12$

Here we present results for the ground state energy per site E_g obtained from the RG fixed point theories for various values of U/t at hole-fraction $f_h = 0$. The values in the third and fifth columns for $U/t = 2, 4, 6, 8, 12$ are obtained from several different numerical methods [11, 44]. The ground state energy values for $U/t = 10$ are obtained from exact diagonalization studies of a 4×4 Hubbard-cluster [45] (table C1).

ORCID iDs

Siddhartha Lal https://orcid.org/0000-0002-5387-6044

References

[1] Lieb E H and Wu F Y 1968 *Phys. Rev. Lett.* **20** 1445
[2] Imada M, Fujimori A and Tokura Y 1998 *Rev. Mod. Phys.* **70** 1039
[3] Anderson P W 1987 *Science* **235** 1196–8
[4] Edegger B, Muthukumar V N and Gros C 2007 *Adv. Phys.* **56** 927–1033
[5] Paramekanti A, Randeria M and Trivedi N 2004 *Phys. Rev.* B **70** 054504
[6] Anderson P W, Lee P, Randeria M, Rice T, Trivedi N and Zhang F 2004 *J. Phys.: Condens. Matter.* **16** R755
[7] Kurosaki Y, Shimizu Y, Miyagawa K, Kanoda K and Saito G 2005 *Phys. Rev. Lett.* **95** 177001
[8] Helton J, Matan K, Shores M, Nytko E, Bartlett B, Qiu Y, Nocera D and Lee Y 2010 *Phys. Rev. Lett.* **104** 147201
[9] Dalla Piazza B *et al* 2015 *Nature Phys.* **11** 62
[10] Iazzi M, Soluyanov A A and Troyer M 2016 *Phys. Rev.* B **93** 115102
[11] LeBlanc J *et al* 2015 *Phys. Rev.* X **5** 041041
[12] Georges A, Kotliar G, Krauth W and Rozenberg M J 1996 *Rev. Mod. Phys.* **68** 13
[13] Georges A and Kotliar G 1992 *Phys. Rev.* B **45** 6479
[14] Werner P and Millis A J 2007 *Phys. Rev.* B **75** 085108
[15] Joo J and Oudovenko V 2001 *Phys. Rev.* B **64** 193102
[16] Moukouri S and Jarrell M 2001 *Phys. Rev. Lett.* **87** 167010
[17] Gull E, Parcollet O and Millis A J 2013 *Phys. Rev. Lett.* **110** 216405
[18] Merino J and Gunnarsson O 2014 *Phys. Rev.* B **89** 245130
[19] Park H, Haule K and Kotliar G 2008 *Phys. Rev. Lett.* **101** 186403
[20] Toschi A, Katanin A and Held K 2007 *Phys. Rev.* B **75** 045118
[21] Held K, Katanin A A and Toschi A 2008 *Prog. Theor. Phys. Suppl.* **176** 117–33
[22] Schäfer T, Geles F, Rost D, Rohringer G, Arrigoni E, Held K, Blümer N, Aichhorn M and Toschi A 2015 *Phys. Rev.* B **91** 125109

[23] Blankenbecler D 1981 *Phys. Rev.* D **24** 2278
[24] Zheng B X and Chan G K L 2016 *Phys. Rev.* B **93** 035126
[25] van Loon E G, Hafermann H and Katsnelson M I 2018 *Phys. Rev.* B **97** 085125
[26] Tocchio L F, Becca F, Parola A and Sorella S 2008 *Phys. Rev.* B **78** 041101
[27] Metzner W, Salmhofer M, Honerkamp C, Meden V and Schönhammer K 2012 *Rev. Mod. Phys.* **84** 299
[28] Tagliavini A, Hille C, Kugler F, Andergassen S, Toschi A and Honerkamp C 2019 *SciPost Phys.* **6** 009
[29] Fu H and Lee D H 2006 *Phys. Rev.* B **74** 174513
[30] Katanin A and Kampf A 2004 *Phys. Rev. Lett.* **93** 106406
[31] Rohe D and Metzner W 2005 *Phys. Rev.* B **71** 115116
[32] Giering K U and Salmhofer M 2012 *Phys. Rev.* B **86** 245122
[33] Hille C, Rohe D, Honerkamp C and Andergassen S 2003 arXiv:2003.01447
[34] Hille C, Kugler F B, Eckhardt C J, He Y Y, Kauch A, Honerkamp C, Toschi A and Andergassen S 2002 arXiv:2002.02733
[35] Głazek S D and Wilson K G 1993 *Phys. Rev.* D **48** 5863
[36] Glazek S D and Wilson K G 1994 *Phys. Rev.* D **49** 4214
[37] Wegner F 1994 *Ann. Phys.* **506** 77–91
[38] Grote I, Körding E and Wegner F 2002 *J. Low Temp. Phys.* **126** 1385–409
[39] Ma S-k, Dasgupta C and Hu C-k 1979 *Phys. Rev. Lett.* **43** 1434
[40] Fisher D S 1992 *Phys. Rev. Lett.* **69** 534
[41] Rademaker L and Ortuno M 2016 *Phys. Rev. Lett.* **116** 010404
[42] You Y Z, Qi X L and Xu C 2016 *Phys. Rev.* B **93** 104205
[43] Pal S, Mukherjee A and Lal S 2019 *New J. Phys.* **21** 023019
[44] Ehlers G, White S R and Noack R M 2017 *Phys. Rev.* B **95** 125125
[45] Dagotto E, Moreo A, Ortolani F, Poilblanc D and Riera J 1992 *Phys. Rev.* B **45** 10741
[46] Anderson P W 1987 *Science* **235** 1196–8
[47] Mukherjee A and Lal S 2019 (https://github.com/anirban-m/anirban-m.github.io/blob/master/unitary-disentanglement-RG/Benchmarking2DHubbard/GroundStateEnergyDensity.ipynb)
[48] Krishnamurthy H, Jayaprakash C, Sarker S and Wenzel W 1990 *Phys. Rev. Lett.* **64** 950
[49] Kemeny G and Caron L G 1967 *Phys. Rev.* **159** 768
[50] Shavitt I and Redmon L T 1980 *J. Chem. Phys.* **73** 5711–7
[51] Suzuki K 1982 *Prog. Theor. Phys.* **68** 246–60
[52] Savitz S and Refael G 2017 *Phys. Rev.* B **96** 115129
[53] Monthus C 2016 *J. Phys. A: Math. Theor.* **49** 305002
[54] Sahin S, Schmidt K P and Orús R 2017 *Europhys. Lett.* **117** 20002
[55] Ortuño M, Somoza A M and Rademaker L 2019 *Phys. Rev.* B **100** 085115
[56] Głazek S D and Wilson K G 2004 *Phys. Rev.* B **69** 094304
[57] Haag R, Hugenholtz N M and Winnink M 1967 *Commun. Math. Phys.* **5** 215–36
[58] Anderson P 1970 *J. Phys. C: Solid State Phys.* **3** 2436
[59] Tallon J and Loram J 2001 *Physica* C **349** 53–68
[60] Imada M, Sakai S, Yamaji Y and Motome Y 2013 Theory of pseudogap in underdoped cuprates *J. Phys.: Conf. Ser.* **449** 012005
[61] Keimer B, Kivelson S A, Norman M R, Uchida S and Zaanen J 2015 *Nature* **518** 179
[62] Anderson P W 1958 *Phys. Rev.* **112** 1900
[63] Volovik G E 2003 *The Universe in a Helium Droplet* vol 117 (Oxford: Oxford University Press)
[64] Sperling J and Vogel W 2011 *Phys. Scr.* **83** 045002
[65] Ruckenstein A and Varma C 1991 *Physica* C **185** 134–40
[66] Sakai S, Motome Y and Imada M 2009 *Phys. Rev. Lett.* **102** 056404
[67] Imada M, Misawa T and Yamaji Y 2010 *J. Phys.: Condens. Matter.* **22** 164206
[68] Anderson P W 1997 A re-examination of concepts in magnetic metals: The 'nearly antiferromagnetic Fermi liquid' *Adv. Phys.* **46** pp 3–11
[69] Moukouri S and Jarrell M 2001 *Phys. Rev. Lett.* **87** 167010
[70] Rozenberg M, Kotliar G and Zhang X 1994 *Phys. Rev.* B **49** 10181
[71] Georges A, Kotliar G, Krauth W and Rozenberg M J 1996 *Rev. Mod. Phys.* **68** 13
[72] Simkovic F, LeBlanc J P F, Kim A J, Deng Y, Prokof'ev N V, Svistunov B V and Kozik E 2020 *Phys. Rev. Lett.* **124** 017003
[73] Varma C, Littlewood P B, Schmitt-Rink S, Abrahams E and Ruckenstein A 1989 *Phys. Rev. Lett.* **63** 1996
[74] Edmonds A R 1985 *The Coupling of Angular Momentum Vectors* (Princeton, NJ: Princeton University Press) pp 31–52
[75] Wen X G 1990 *Int. J. Mod. Phys.* B **4** 239–71
[76] Oshikawa M and Senthil T 2006 *Phys. Rev. Lett.* **96** 060601
[77] Chen X, Gu Z C and Wen X G 2010 *Phys. Rev.* B **82** 155138
[78] Salmhofer M, Honerkamp C, Metzner W and Lauscher O 2004 *Prog. Theor. Phys.* **112** 943–70
[79] Furukawa N, Rice T and Salmhofer M 1998 *Phys. Rev. Lett.* **81** 3195
[80] Binz B, Baeriswyl D and Douçot B 2002 *Eur. Phys. J.* B **25** 69–87
[81] Irkhin V Y, Katanin A and Katsnelson M 2001 *Phys. Rev.* B **64** 165107
[82] Fradkin E 2013 *Field Theories of Condensed Matter Physics* (Cambridge: Cambridge University Press)
[83] Tocchio L F, Becca F and Sorella S 2016 *Phys. Rev.* B **94** 195126
[84] Sakai S, Motome Y and Imada M 2010 *Phys. Rev.* B **82** 134505
[85] Kawasaki S, Li C, Kuhns P L, Reyes A P and Zhang G 2010 *Phys. Rev. Lett.* **105** 137002
[86] Mukherjee A and Lal S 2020 *New J. Phys.* **22** 063008
[87] Randeria M and Taylor E 2014 *Annu. Rev. Condens. Matter Phys.* **5** 209
[88] Mukherjee B, Patel P B, Yan Z, Struck J and Zwierlein M W 2019 *Phys. Rev. Lett.* **122** 203402
[89] Yu Y, Ma L, Cai P, Zhong R, Ye C, Shen J, Gu G D, Chen X H and Zhang Y 2019 *Nature* **575** 156–63
[90] Auerbach A 2012 *Interacting Electrons and Quantum Magnetism* (Berlin: Springer)
[91] Halboth C J and Metzner W 2000 *Phys. Rev.* B **61** 7364
[92] Halboth C J and Metzner W 2000 *Phys. Rev. Lett.* **85** 5162